

1 **r.randomwalk v1, a multi-functional conceptual tool for** 2 **mass movement routing**

3

4 **Martin Mergili^{1,2}, Julia Krenn^{2,3} and Hone-Jay Chu⁴**

5

6 [1]{Geomorphological Systems and Risk Research, Department of Geography and Regional
7 Research, University of Vienna, Universitätsstraße 7, 1190 Vienna, Austria}

8 [2]{Institute of Applied Geology, University of Natural Resources and Life Sciences
9 (BOKU), Peter-Jordan-Straße 70, 1190 Vienna, Austria}

10 [3]{Department of Geological Sciences, University of Canterbury, Private Bag 4800,
11 Christchurch, New Zealand}

12 [4]{Department of Geomatics, National Cheng Kung University, 1 University Road, Tainan
13 701, Taiwan}

14 Correspondence to: M. Mergili (martin.mergili@boku.ac.at)

15

16 **Abstract**

17 We introduce r.randomwalk, a flexible and multi-functional open source tool for backward-
18 and forward-analyses of mass movement propagation. r.randomwalk builds on GRASS GIS,
19 the R software for statistical computing and the programming languages Python and C. Using
20 constrained random walks, mass points are routed from defined release pixels of one to many
21 mass movements through a digital elevation model until a defined break criterion is reached.
22 Compared to existing tools, the major innovative features of r.randomwalk are: (i) multiple
23 break criteria can be combined to compute an impact indicator score; (ii) the uncertainties of
24 break criteria can be included by performing multiple parallel computations with randomized
25 **parameter sets**, resulting in an impact indicator index in the range 0–1; (iii) built-in functions
26 for validation and visualization of the results are provided; (iv) observed landslides can be
27 back-analyzed to derive the density distribution of the observed angles of reach. This
28 distribution can be employed to compute impact probabilities for each pixel. Further, impact
29 indicator scores and probabilities can be combined with release indicator scores or

1 probabilities, and with exposure indicator scores. We demonstrate the key functionalities of
2 r.randomwalk (i) for a single event, the Acheron Rock Avalanche in New Zealand; (ii) for
3 landslides in a 61.5 km² study area in the Kao Ping Watershed, Taiwan; and (iii) for lake
4 outburst floods in a 2,106 km² area in the Gunt Valley, Tajikistan.

5 Keywords: Conceptual model, GIS raster analysis, mass movements, open source, random
6 walk

7

8 **1 Introduction**

9 Mass movement processes such as landslides, debris flows, rock avalanches or snow
10 avalanches may lead to damages or even disasters when interacting with society. Computer
11 models predicting travel distances, hazardous areas, impact energies or travel times may help
12 the society to mitigate the effects of such processes and, consequently, to reduce the risk and
13 the losses (Hungr et al., 2005).

14 Physically-based dynamic models are used for in-detailed analyses of specific events or
15 situations (e.g., Savage and Hutter, 1989; Takahashi et al., 1992; Iverson, 1997; Pudasaini and
16 Hutter, 2007; McDougall and Hungr, 2004, 2005; Pitman and Le, 2005; Christen et al.,
17 2010a, b; Mergili et al., 2012b; Pudasaini, 2012; Hergarten and Robl, 2015; Mergili et al.,
18 2015). Since the processes are complex in detail and the input parameters are uncertain,
19 simplified conceptual models for the motion of mass flows are today used in combination
20 with GIS. These models may be used for single events. However, they are particularly useful
21 to indicate potential impact areas at broader scales. Hypothetic mass points are routed from a
22 release pixel through a digital elevation model (DEM) until a defined break criterion is
23 reached. Monte Carlo techniques (random walks, Pearson, 1905; Gamma 2000) or multiple
24 flow direction algorithms (Horton et al., 2013) are employed to simulate the lateral spreading
25 of the flow.

26 The break criteria often consist in threshold values of the angle of reach (i.e., the average
27 slope of the path) or horizontal and vertical distances (Lied and Bakkehøi, 1980; Vandre,
28 1985; McClung and Lied, 1987; Burton and Bathurst, 1998; Corominas et al., 2003; Haeberli,
29 1983; Zimmermann, 1997; Huggel et al., 2002, 2003, 2004a, b), sometimes related to volume
30 (Rickenmann, 1999; Scheidl and Rickenmann, 2009) are used as criteria. The scatter in the

1 relationships is usually large. Using the worst case may be an appropriate first estimate, but is
2 often too conservative for design issues (Hungri et al., 2005).

3 Some approaches include simplified physically-based models going back to the mass flow
4 model of Voellmy (1955), relating the shear traction to the square of the velocity and
5 assuming an additional Coulomb friction effect (Pudasaini & Hutter, 2007). They consider
6 only the centre of the flowing mass, but not its deformation and the spatial distribution of the
7 flow variables. This type of models is mainly used for snow avalanches and debris flows
8 (Perla et al., 1980; Gamma, 2000; Wichmann and Becht, 2003; Fischer et al., 2012; Mergili et
9 al., 2012a; Horton et al., 2013).

10 Various – mostly open source – software tools for conceptual modelling of mass movements
11 (mainly flows) at medium or broad scales are available (e.g., Gamma, 2000; Wichmann &
12 Becht 2003; Mergili et al. 2012a; Horton et al., 2013). However, most of these tools are
13 lacking substantial features: (i) they are limited to one single type of break criterion; (ii) they
14 do not allow to directly account for the uncertainty of the break criteria; (iii) they do not allow
15 to back-calculate the statistics of a set of observed mass movements; (iv) they do not offer
16 built-in functionalities for evaluating the model results against observations. Consequently,
17 the key objectives of the present study are:

- 18 • To introduce r.randomwalk, a freely available, comprehensive and flexible tool for
19 routing mass movements;
- 20 • To demonstrate the various functionalities of r.randomwalk, particularly in terms of
21 overcoming the issues (i)–(iv);
- 22 • To discuss the potentials and limitations of this tool.

23 Next, we will describe the r.randomwalk software tool (Sect. 2). Then we will present **the test**
24 **areas and the results** (Sect. 3). We will discuss the findings (Sect. 4) and conclude with some
25 key messages of the work (Sect. 5).

26

1 2 The r.randomwalk application

2 2.1 Computational implementation

3 r.randomwalk is implemented as a raster module of the open source software package GRASS
4 GIS 7 (Neteler and Mitasova, 2007; GRASS Development Team, 2015). We use the Python
5 programming language for data management, pre-processing and post-processing tasks
6 (module r.randomwalk). The routing procedure (see Sect. 2.2–2.4) is written in the C
7 programming language (sub-module r.randomwalk.main). The R software environment for
8 statistical computing and graphics (R Core Team, 2015) is employed for built-in validation
9 and visualization functions (see Sect. 2.5). Parallelization of multiple model runs is enabled. It
10 allows the exploitation of all computational cores available, speeding up analysis processes.
11 The parallelization procedure is implemented at the Python level (analogous to the way
12 described in Mergili et al., 2014): the module r.randomwalk produces a batch file for each
13 model run. This batch file calls the Python-based sub-module r.randomwalk.mult, which is
14 then used to launch r.randomwalk.main with the specific parameters for the associated model
15 run. Thereby, the Python library “Threading”, a higher-level threading interface, and the
16 Python module “Queue”, a class helping to block execution until all the items in the queue
17 have been processed, are exploited. Parallel processing serves for reducing the computational
18 time in the following contexts:

- 19 • Analyses with multiple random subsets of the release areas or coordinates. In each
20 model run, one subset is used for back-calculating the probability density function
21 (PDF) of the angle of reach, the other subset is employed for validating the
22 distribution of the impact probability derived with this PDF against the observed
23 deposition areas;
- 24 • Analyses with multiple combinations of input parameters varied in a controlled or
25 randomized way, enabling to consider parameter uncertainties and to explore
26 parameter sensitivity.

27 r.randomwalk was developed and tested with Ubuntu 12.04 LTS and is expected to work on
28 other UNIX systems, too. A simple user interface is available. However, the tool may be
29 started more efficiently through command line parameters, enabling a straightforward
30 batching on the shell script level. This feature facilitates model testing, the combination with
31 other GRASS GIS modules and the consideration of process chains (i.e., using the output of

1 one analysis as the input for the next one). The logical framework is illustrated in Fig. 1, the
2 key variables used in `r.randomwalk` are summarized in Table 1.

3 **2.2 Random walk routing**

4 The term random walk refers to a Monte-Carlo-approach for routing an object through any
5 type of space. The term was introduced by Pearson (1905). Constrained random walk
6 approaches are used for routing mass movements such as debris flows through elevation maps
7 (DEMs) e.g., by Gamma (2000), Wichmann and Becht (2003), Mergili et al. (2012a) and
8 Gruber and Mergili (2013). Such methods enable a certain degree of spreading of the
9 movement by considering also other routing directions than the steepest descent. It avoids the
10 concentration of flows – or any other types of mass movements – to linear features which
11 would not be realistic for debris flows, snow avalanches or other types of mass movements.
12 However, the routing is constrained or weighted by factors such as the slope or the
13 perpetuation of the flow direction. An alternative to constrained random walk routing would
14 consist in a multiple flow direction algorithm (Horton et al., 2013).

15 In the context of `r.randomwalk`, each random walk routes a hypothetical mass point from a
16 release pixel through the DEM until a break criterion is reached (see Sect. 2.3). A large set of
17 random walks is required for each mass point in order to achieve a satisfactory cover of the
18 possible impact area. `r.randomwalk` is designed for:

- 19 • One set of random walks for one mass movement, starting from a defined set of
20 coordinates.
- 21 • Multiple sets of random walks for one mass movement, one set starting from each
22 pixel of the release area.
- 23 • Sets of random walks for multiple mass movements in a study area (either starting
24 from one set of coordinates per mass movement, or from all pixels defined as release
25 areas).
- 26 • One set of random walks starting from each pixel in the study area.

27 Overlay rules for different random walks and sets of random walks are applied (see Sect. 2.4).

28 During the pixel-to-pixel routing procedure, turns of $>90^\circ$ are not supported. Neighbour pixels
29 are further considered invalid as target pixels in case they are out of the study area or conflict
30 with at least one of the following requirements:

- Eq. (1) allows upward movements. In order to constrain upward movements, a user-defined maximum vertical run-up height R_{\max} is introduced. It takes the lowest elevation the random walk has passed through as reference.
- Certain types of mass flows (i.e., those with high viscosity) hardly change their flow direction sharply. The user-defined horizontal control distance L_{ctrl} defines the backward distance of each step over which the horizontal distance of motion has to increase (Fig. 2A).

The probability P_{px} of any other neighbour pixel px to become the target pixel is

$$P_{\text{px}} = p_{\text{px}} / \sum_{q^x=1}^{q^x=n} p_{q^x}, p = f_d e^{f_\beta \tan \beta}, \quad (1)$$

where n is the total number of valid neighbour pixels, and β is the local slope between the current pixel and the considered neighbour pixel. f_d and f_β are weighting factors for the perpetuation of the flow direction and for the slope. f_d is governed by the input parameter d : $f_d = d^2$ for the same flow direction as the previous one, $f_d = d$ for a 45° turn and $f_d = 1$ for a 90° turn.

The break criteria for the random walks (see Sect. 2.3) are directly or indirectly related to the travel distance L_{\max} i.e., the horizontal length between the release pixel and the terminal pixel measured along the flow path. Preliminary tests reveal that random walk routing through raster maps may result in quite uneven flow paths (see Fig. 2B). Consequently, the distance calculated by summing up all the pixel-to-pixel distances may be significantly longer than the more relevant distance along the observed main flow paths. Employing the sums of the pixel-to-pixel distances would lead to an underestimation of the angle of reach and, consequently, of the predicted travel distances and impact areas. We approach this problem by dividing the flow paths into straight segments with a user-defined maximum length of L_{seg} . The travel distance L_{\max} is defined as the sum of the length of all segments (see Fig. 2B). Larger values of L_{seg} are expected to result in shorter travel distances due to the more pronounced smoothing of the path.

2.3 Break criteria

Each random walk continues until at least one neighbour pixel is outside the study area, or until the user-defined break criterion is fulfilled. The break criteria are the key parameters for estimating the mass flow impact areas and can be defined in various ways (Table 2):

- 1 • The angle of reach ω_T or the maximum travel distance L_{\max} is computed from
2 empirical-statistical rules or relationships, based on the analysis of observed events
3 (Table 3). They usually refer to the distance between the highest spot of the release
4 area and the most distant spot of the impact area along the flow path (the
5 “Fahrböschung” according to Heim, 1932). Consequently, random walks using this
6 type of break criterion have to start from the set of coordinates defining the highest
7 point of the observed or expected mass movement. Alternatively, also a semi-
8 deterministic model (Perla et al., 1980) can be used.
- 9 • Empirical-statistical relationships or the semi-deterministic model may be applied in a
10 large number of parallel computations with randomized values of the parameters a , b
11 and c (see Fig. 1 and Table 3). This allows to explore the effects of uncertainties in the
12 relationships. Only one type of relationship is considered at once, and the output
13 consists in a raster map of the impact indicator index III in the range 0–1, representing
14 the fraction of tested parameter combinations predicting an impact on the pixel (i.e.,
15 where $III = 1$). Further, the results of all model runs are stored in a way ready to be
16 analyzed with the parameter sensitivity & optimization tool AIMEC (Automated
17 Indicator based Model Evaluation and Comparison; Fischer, 2013).
- 18 • An impact probability raster map P_I in the range 0–1 is computed from a user-defined
19 sample of observed values of $\tan(\omega_T)$ which is employed to build a cumulative density
20 function (CDF). The CDF represents the probability that the movement reaches the
21 pixel associated to each value of $\tan(\omega_T)$. The sample of observed values may be
22 divided into one subset of mass movements for building the CDF, and another one for
23 computing P_I . This ensures a clear separation between parameter optimization and
24 model validation (see Sect. 2.5). Parallel processing may be used to repeat the analysis
25 for many random subsets in order to achieve a more robust result.
- 26 • If an inventory of events is available, the observed impact areas may be back-
27 calculated by routing each random walk until it leaves the observed impact area of the
28 corresponding mass movement. This mode can be used to explore the statistical
29 distribution of ω_T . The resulting CDF can be used as input to estimate P_I .

1 2.4 Overlay of random walk results

2 Each random walk does not stand for itself alone. Instead, it has to be overlaid with other
3 random walks at two levels:

- 4 1. Random walks of the same mass point: IF is increased by 1 for each random walk
5 predicting an impact. IIS is increased by 1 for each model where at least 1 random
6 walk predicts an impact. The average angle of path – and therefore also P_1 – are
7 derived from the random walk with the shortest travel distance (i.e., the straightest
8 flow path and the highest value of ω) at the considered pixel.
- 9 2. Sets of random walks for different mass points: the values of IF for all random walks
10 impacting a pixel are just added up whilst the maximum of IIS is applied to each pixel.
11 The issue gets more complex when it comes to P_1 : depending on the specific
12 application, the maximum or the average out of all sets of random walks is more
13 appropriate.

14 The resulting maps of P_1 or IIS can be automatically overlaid with a release probability P_R
15 (result: composite probability P_{LC} ; Mergili and Chu, 2015) or a release indicator score RIS
16 (result: impact hazard indicator score $IHIS$), and with an exposure indicator score EIS derived
17 from the land cover (result: impact risk indicator score $IRIS$; see Table 1). These steps are not
18 further considered in this article and are therefore not shown in Fig. 1.

19 2.5 Validation

20 r.randomwalk includes three possibilities for validation of the model results. All three build
21 on the availability of a raster map of the observed deposition area of the mass movement(s)
22 under investigation. All parts of the observed impact areas outside of the observed deposition
23 areas are set to no data (Fig. 3).

- 24 • For IIS , the true positive (TP), true negative (TN), false positive (FP) and false
25 negative (FN) predictions are counted on the basis of pixels and put in relation. All
26 pixels with $IIS \geq 1$ are considered as observed positives (OP), all pixels with $IIS = 0$
27 are considered as observed negatives.
- 28 • ROC (Receiver Operating Characteristics) Plots are produced for III or P_1 : the true
29 positive rate r_{TP} (TP/OP) is plotted against the false positive rate r_{FP} (FP/ON) for
30 various levels of III or P_1 . The area under the curve connecting the resulting points,
31 AUC_{ROC} , is used as an indicator for the quality of the prediction (see Fig. 3). If the

1 CDF for P_I is derived from the same set of landslides, r.randomwalk includes the
2 option to randomly split the set of observed landslides into a set for **parameter**
3 **optimization**, and one for validation. This is done for a user-defined number of times,
4 exploiting multiple processors (see Sect. 2.3 and Fig. 1). It results in an ROC Plot with
5 multiple curves. **Note that two ROC Plots are produced: one of them builds on the**
6 **original number of TN pixels. For the other one the number of ON pixels is set**
7 **to 5 times the number of OP pixels. Whilst the number of FP pixels remains**
8 **unchanged, the number of TN pixels is modified accordingly. This procedure aims at**
9 **normalizing the ROC curves in order to enable a comparison of the prediction**
10 **qualities yielded for different study areas.**

- 11 • If only one mass movement is considered, a longitudinal profile may be defined by a
12 set of coordinates of the profile vertices. The observed and predicted ($III \geq 1$ or
13 $P_I > 0$) travel distances are measured and compared along this profile.

15 3 Test cases and results

16 3.1 Acheron Rock Avalanche, New Zealand

17 3.1.1 Area description and model parameterization

18 The Acheron Rock Avalanche in Canterbury, New Zealand (Fig. 4), was triggered approx.
19 1,100 years BP (Smith et al., 2006). Within the present study, the release volume
20 $V = 6.4$ million m^3 is approximated from the reconstruction of the pre-failure topography and
21 is lower than the value of $V = 7.5$ million m^3 estimated by Smith et al. (2006). We use a 10 m
22 resolution DEM derived by stereo-matching of aerial photographs. Impact, release and
23 deposition areas are derived from field and imagery interpretation as well as from data
24 published by Smith et al. (2006). All random walks start from the highest pixel of the release
25 area.

26 We use this case study for demonstrating how to compute the impact indicator index III from
27 an elevation map, the release area and the release volume. Before doing so, we have to
28 analyze the influence of the pixel size and the parameters n_{walks} , R_{max} , L_{ctrl} , L_{seg} , f_β and f_d on the
29 model result. Preliminary tests have shown that r.randomwalk yields plausible results with the
30 number of random walks $n_{walks} = 10^4$, $R_{max} = 10$ m, $L_{ctrl} = 1000$ m, $L_{seg} = 100$ m, $f_\beta = 5$, $f_d = 2$,

1 and a pixel size of 20 m. These values are taken as a basis to explore the sensitivity of the
2 model results to the variation of each parameter and the best fit of the parameters in terms of
3 the travel distance, AUC_{ROC} and the size of the predicted impact area (Table 4). $\omega_T = 11.62^\circ$,
4 the angle of reach observed for the Acheron Rock Avalanche, is applied as the break criterion
5 for all tests. Some of the tests are run in the back-calculation mode (flag b; see Tables 2
6 and 4).

7 III is computed by executing `r.randomwalk` for 100 times with the parameter values optimized
8 according to Table 4. We explore an empirical-statistical relationship for ω_T derived from a
9 compilation of 127 case studies (Fig. 5). The offset of the equation (b in Eq. 4 and Fig. 5) is
10 randomly sampled between the lower and upper envelopes of the regression. The quality of
11 the prediction is evaluated using **the** ROC Plot (see Figs. 1 and 3). Note that the Acheron
12 Rock Avalanche (not included in the relationship developed in Fig. 5) is found close to the
13 lower envelope, meaning that it was very mobile compared to most of the other events.

14 3.1.2 Results

15 Fig. 6 summarizes the findings of the Tests 1–3 (see Table 4). Test 1 leads to the expected
16 result that the predicted impact area increases with the number of random walks. However,
17 the predicted impact area is also a function of the pixel size: with larger pixels, less random
18 walks are needed to cover an area of similar size than with smaller pixels. Fig. 6A further
19 indicates that the possible impact area is not fully covered even at 10^5 random walks: no
20 substantial flattening of the curves is observed. We conclude that (i) a very high value of
21 n_{walks} would be necessary to fully cover the possible impact area, and (ii) this would lead to a
22 substantial overestimation of the observed impact area.

23 On the other hand, the quality of the prediction in terms of AUC_{ROC} reaches a **maximum** at
24 $n_{walks} \approx 10^2$ (pixel size 40 m) or $n_{walks} \approx 10^3$ (pixel size 20 m), **decreasing** with higher values of
25 n_{walks} . **At a pixel size of 10 m, AUC_{ROC} reaches a constant level at $n_{walks} \approx 10^4$** (see Fig. 6B).
26 We may conclude that excessive numbers of random walks lead to an overestimation of the
27 impact area rather than to a better prediction quality. Coarser pixel sizes allow to achieve the
28 same level of coverage and the same prediction quality at lower values of n_{walks} . However, the
29 pixel size has to be fine enough to account for the main geometric characteristics of the
30 process under investigation (see Sect. 4). All further tests are performed with $n_{walks} = 10^4$.

1 Fig. 6C illustrates that, at $L_{ctrl} = 1000$ m, the travel distance computed within the observed
2 impact area decreases with increasing values of L_{seg} (Tests 2 and 3 in Table 4). This pattern is
3 well explained by Fig. 2B. At short segment lengths, the effects of flow paths frequently
4 **changing their direction** are particularly evident for pixel sizes of 10 m and 20 m. L_{max} drops
5 below the observed value of 3550 m (see Fig. 4B) at **$75 \leq L_{seg} \leq 100$ m**. With $L_{seg} \geq 3050$ m,
6 corresponding to the Euclidean distance between the release point and the terminal point of
7 the Acheron Rock Avalanche, L_{max} would also take a value of 3050 m. At $L_{ctrl} = 50$ m (only
8 shown for a pixel size of 20 m), r.randomwalk tends to predict too long travel distances,
9 compared to the observation. This phenomenon occurs as flow directions are not well defined
10 in the relatively plane deposition zone of the Acheron Rock Avalanche, so that flow paths
11 may frequently **change** their direction or even go backwards or in a circular way if such a
12 behaviour is not impeded by sufficiently high values of L_{ctrl} (see Fig. 2A). Fig. 6D indicates
13 that this undesired behaviour (visible in the area marked by the X in the gray circle)
14 disappears at $L_{ctrl} > 200$ m.

15 On the other hand, the value of L_{ctrl} should not be chosen too high as this may negatively
16 impact the model performance. In the case of the Acheron Rock Avalanche, a drop in
17 AUC_{ROC} is observed between $L_{ctrl} \approx 2000$ and **$L_{ctrl} \approx 2500$ m** (Fig. 7A). This drop is explained
18 by an increasing number of false negative pixels in those areas which cannot be reached by
19 the random walks due to **the** strict constraint of flow direction.

20 Within the tested ranges of parameter values, the quality of the prediction is highest at values
21 of **$R_{max} \approx 5-10$ m** (see Fig. 7B) and **$f_{\beta} \geq 5$** (see Fig. 7C) whilst it **reaches its maximum at $f_d \approx 2-$**
22 **3** (see Fig. 7D). The predicted impact area increases with increasing R_{max} and f_d whilst it
23 decreases with increasing f_{β} .

24 Figs. 6 and 7 indicate that the initial values of n_{walks} , L_{ctrl} , L_{seg} , R_{max} , f_{β} , f_d , and the pixel size
25 suggested in Sect. 3.1.1 and Table 4 are within the optimum range of values (see Sect. 4).
26 Therefore, they are used for computing the impact indicator index for the Acheron Rock
27 Avalanche (Fig. 8A). Concerning the break criteria, this can be classified as a forward
28 analysis. As expected from Fig. 5, where the Acheron Rock Avalanche falls in between the
29 envelopes of the relationship employed, the upper part of the observed impact area displays a
30 value of $III = 1$, whilst the remaining part of the observed impact area displays values of
31 $1 > III > 0$, decreasing towards the terminus. As the event was comparatively mobile within
32 the context of the relationship used (see Sect. 3.1.1 and Fig. 5), the values of III are close to

1 zero in the terminal area, and the area with $III > 0$ does not reach far beyond the observed
2 terminus. Note that the maximum value of III is 0.8, meaning that 20% of all model runs did
3 not even start due to very high values of ω_T yielded with the randomized values of b (see
4 Fig. 5). Evaluation against the observed deposit yields a value of $AUC_{ROC} = 0.94$ (see
5 Fig. 8B). All values of AUC_{ROC} shown in the Figs. 6 and 7 and the ROC Plot of Fig. 8B build
6 on normalized ON areas (see Sect. 2.5).
7 III was generated within a computational time of 188 seconds, employing a machine with
8 eight cores.

9 3.2 Kao Ping Watershed, Taiwan

10 3.2.1 Area description and model parameterization

11 Between 7 and 9 August 2009, Typhoon Morakot struck Taiwan and triggered enormous
12 landslides, causing significant land cover change (Fig. 9). More than 22,000 landslides were
13 recorded in Southern Taiwan (Lin et al., 2011). One of the hot spots of mass wasting was the
14 Kao Ping Watershed (Wu et al., 2011), where the extremely heavy rainfall (in total, more than
15 2000 mm depth and 90 h duration) triggered a catastrophic landslide in the Hsiaolin Village
16 (Kuo et al., 2013).

17 We consider a 61.5 km² subset of the Kao Ping Watershed for computing the landslide impact
18 probability P_I , based on the observed landslide release areas. 207 landslides are mapped in the
19 shale, sandstone and colluvium slopes. (see Fig. 9). A 10 m DEM is used along with an
20 inventory of the landslide impact areas. Release and deposition areas are extracted from the
21 inventory. We employ the values of n_{walks} , R_{max} , f_{β} , f_d , L_{ctrl} , L_{seg} resulting from the optimization
22 procedure for the Acheron Rock Avalanche (see Sect. 3.1.1), and a pixel size of 20 m. P_I is
23 computed as follows:

- 24 1. A set of random walks ($n_{walks} = 10^4$) is started from each release point (i.e., the highest
25 pixel of each landslide). Each random walk stops as soon as it would leave the impact
26 area of the same landslide (back-calculation, flag b).
- 27 2. After completing all random walks for the study area, the statistical distribution of ω_T
28 is analyzed. All landslides with $L_{max} < 100$ m are excluded. A fraction of 20% out of
29 all landslides (i.e., all values of ω_T associated with those landslides) is randomly
30 selected and retained for validation. Using visual comparison, we have identified the

1 log-normal distribution as the most suitable type of distribution for this purpose.

2 Consequently, the log-normal cumulative density function (CDF) stands for the
3 probability that a moving mass point leaves the observed impact area at or below the
4 associated threshold of ω_T .

5 3. We perform a forward analysis of P_I by starting a set of random walks ($n_{\text{walks}} = 10^4$)
6 from the release points of the retained landslides, and assigning the cumulative density
7 associated to the average angle of path to each pixel. The result is validated against the
8 observed deposition zones of the retained landslides by means of an ROC Plot.

9 4. 2. and 3. are repeated for 100 randomly selected subsets (parallel processing is
10 applied). The final map of P_I is generated by applying for each pixel the maximum of
11 the values yielded by all the model runs.

12 We refer to this work flow as Test 1 and repeat the analysis with starting random walks not
13 only from the release points, but from all the pixels within the observed release areas (Test 2).
14 This means that the CDF is derived from a much larger sample of data than when considering
15 only one point per landslide for starting random walks. We exclude all sets of random walks
16 yielding $L_{\text{max}} < 100$ m, use a log-normal CDF and start a set of only 10^3 random walks from
17 each release pixel for computing P_I .

18 3.2.2 Results

19 Starting sets of 10^4 random walks from the highest points of all landslides (Test 1) results in a
20 range of values of $16.0 \leq \omega_T \leq 43.5^\circ$, an average of 30.4° and a standard deviation of 5.2°
21 (derived from $n = 132$ landslides, excluding those with $L_{\text{max}} < 100$ m). Repeating the analysis
22 with 10^4 random walks started from each pixel within the landslide release areas (Test 2) we
23 observe a range of values $16.4 \leq \omega_T \leq 44.1^\circ$, an average of 26.9° and a standard deviation of
24 4.8° ($n = 1563$). Fig. 10 illustrates the histograms, probability density and cumulative density
25 functions derived from both analyses. Even though the ranges of values are similar in both
26 tests, Test 1 yields (i) a higher average of ω_T and (ii) a broader range of values than Test 2. (i)
27 is explained by the fact that those random walks starting from lower parts of the release areas
28 are expected to leave the observed impact area at lower values of ω_T . (ii) is most likely the
29 consequence of a number of rather small landslides with high or low values of ω_T strongly
30 reflected in the statistics. Such outliers are less prominent in the statistics of Test 2 due to the
31 much higher number of cases, most of them related to the larger landslides.

1 Each of the impact probabilities shown in Fig. 11 represents the overlay of 100 analyses
2 where random sets of 80% of the landslides are used for deriving the CDF and the remaining
3 20% are used for computing the impact probabilities. The maps illustrate the maximum values
4 of P_1 out of the overlay of the 100 results. Each of the results is derived using a slightly
5 different CDF. Both tests yield largely similar patterns of P_1 . We note that (i) Test 2 predicts
6 larger impact areas and higher values of P_1 than Test 1, and (ii) some random walks take the
7 “wrong” direction in Test 2 (indicated by “1” in the yellow circle in Fig. 11B), a phenomenon
8 not observed for Test 1. (i) is explained by the higher number – and the broader distribution –
9 of release pixels in Test 2, compared to Test 1. The reason for (ii) is that random walks
10 starting from the highest point of an observed landslide are forced to flow into the observed
11 landslide area (Test 1), a constraint not applicable when starting random walks from each
12 release pixel (Test 2). In this case it happens that pixels located at or near a crest produce
13 random walks in both directions. In Test 1, the computational time amounted to 63 seconds
14 for deriving the CDF and 8613 seconds for calculating P_1 , employing a machine with eight
15 cores. In Test 2, these times increased to 1719 and 9752 seconds, respectively. The relatively
16 slight increase with regard to P_1 results from the reduced value of n_{walks} in Test 2.

17 The prediction quality is tested for each of the 100 model runs for the two tests, producing
18 sets of 100 ROC Curves (Fig. 12). $AUC_{\text{ROC}} = 0.917 \pm 0.038$ for Test 1 and 0.920 ± 0.029 for
19 Test 2, both computed with the original number of TN pixels (see Sect. 2.5).

20 In contrast, the procedures demonstrated in the two tests vary strongly in their scope of
21 applicability. We have demonstrated the methodologies by back-calculating observed
22 landslides. As soon as this is done, one may go one step further:

- 23 • The methodology shown in Test 1 can be employed to make forward predictions for
24 defined expected future landslides, given that a sufficient set of observed landslides of
25 similar behaviour is available to derive the CDF.
- 26 • The methodology demonstrated in Test 2 can be used in combination with maps of
27 landslide release probability to explore the composite probability of a landslide impact
28 (see Sect. 2.4 and 4).

29 In either case the statistics (see Fig. 10) have to be derived with the same type of approach
30 later used for producing the P_1 map.

31

1 3.3 Gunt Valley, Tajikistan

2 3.3.1 Area description and model parameterization

3 As most mountain areas worldwide, the Pamir of Tajikistan experiences a significant retreat
4 of the glaciers. One of the consequences thereof consists in the formation and growth of lakes,
5 some of which are subject to glacial lake outburst floods (GLOFs) which may evolve into
6 destructive debris flows (Mergili and Schneider, 2011; Mergili et al., 2013; Gruber and
7 Mergili, 2013). No records of historic GLOFs in the test area are known to the authors.
8 However, in August 2002 a GLOF in the nearby Shakh dara Valley evolved into a debris flow
9 which destroyed the village of Dasht, claiming dozens of lives (Mergili et al., 2011).

10 The frequency of such events is low and historical data are sparse. Consequently, possible
11 travel distances of GLOFs may not be derived in a purely statistical way. Instead, we have to
12 use published empirical-statistical relationships and simple rules to produce an impact
13 indicator score (*IIS*) map.

14 We compute *IIS* with regard to GLOFs for a 2,106 km² study area in the Gunt Valley
15 (Fig. 13). The analysis builds on the ASTER GDEM V2 and the coordinates and
16 characteristics (estimates of V and Q_p) of 113 lakes in the area (Gruber and Mergili, 2013).

17 A set of random walks ($n_{\text{walks}} = 10^4$) is routed from the outlet of each lake through the DEM.
18 Six break criteria are combined to compute *IIS*, partly following Gruber and Mergili (2013).
19 The relationships and rules employed as **break** criteria are summarized in Table 5. Rule 1 is
20 applied with $\omega_T = 11^\circ$ (Test 1 – according to Haeberli, 1983; Huggel et al., 2003, 2004 for
21 debris flows from glacier- or moraine-dammed lakes; Zimmermann et al., 1997 for coarse-
22 and medium-grained debris flows) and with $\omega_T = 7^\circ$ (Test 2 – Zimmermann et al., 1997 for
23 fine-grained debris flows). All other rules and relationships are used for both tests. For each
24 pixel, *IIS* consists in the number of relationships or rules predicting an impact (i.e., *IIS* takes
25 values in the range 0–6).

26 R_{max} , L_{ctrl} , L_{seg} , f_β and f_d are set to the optimum values found for the Acheron Rock Avalanche,
27 the pixel size is set to 60 m.

28 3.3.2 Results

29 Fig. 14 illustrates the possible impact areas of GLOFs in the Gunt Valley study area according
30 to the relationships listed in Table 5.

1 Fig. 14A shows the impact indicator score IIS i.e., the number of relationships predicting an
2 impact, resulting from Test 1 (rule 1 applied with $\omega_T = 11^\circ$). Except for one prominent
3 exception, $IIS > 3$ (possible debris flow impact) only for the largely uninhabited upper
4 portions of the tributaries to the Gunt Valley. In contrast, a possible flood impact ($1 \leq IIS \leq 3$)
5 is predicted for much of the main valley. Test 2 (rule 1 applied with $\omega_T = 7^\circ$) predicts a
6 possible debris flow impact also for part of the main valleys (see Fig. 14B). The impact
7 frequency IF (per cent of random walks impacting each pixel) for Test 1 is shown in Fig. 14C
8 for a subsection of the test area, classified by quantiles. IF is strongly governed by the width
9 of the movement i.e., by the local topography, and may serve as a surrogate for the expected
10 depth rather than as for the probability of an impact.

11 Note that Fig. 14 only indicates the tendency of an already released GLOF to impact certain
12 pixels. It does not provide any information on the susceptibility of a certain lake to produce a
13 GLOF at all. Earlier, Mergili and Schneider (2011) and Gruber and Mergili (2013) have
14 attempted to combine GLOF release indicators with impact indicators and land cover maps to
15 generate hazard and risk indicator maps. However, the results of their studies may
16 underestimate the possible impact areas as the travel distance was computed on a pixel-to-
17 pixel basis, possibly yielding too low values of ω_T (see Figs. 2 and 6).

18 The robustness and appropriateness of the rules and relationships for low-frequency events
19 such as GLOFs (see Table 5) is questionable. The rules building on a unique value of ω_T
20 overpredict the possible impact areas for those lakes where not enough water is available to
21 produce a flood in downstream valleys. Applying the rules and relationships for debris flows
22 implies a blind assumption that enough entrainable sediment is available to produce a debris
23 flow. Whilst $\omega_T \geq 11^\circ$ is considered the worst case for debris flows of GLOFs from glacier-
24 or-moraine-dammed lakes in the European Alps according to Haeberli (1983) and
25 Huggel et al. (2002), $\omega_T = 9.3^\circ$ was measured for the 2002 Dasht Event, the only well-
26 documented GLOF near the test area (Mergili et al., 2011). Also the relationship proposed by
27 Rickenmann (1999) severely underestimates the travel distance of this event, even when
28 massive bulking is assumed. Applying $\omega_T = 7^\circ$ as given by Zimmermann (1997) for fine-
29 grained debris flows might be more suitable as worst-case assumption for debris flows from
30 GLOFs in the Pamir, even though this threshold leads to very conservative predictions.

31 We have measured computational times of 1520 seconds for Test 1 and 1556 seconds for
32 Test 2, using a machine with eight cores.

1

2 **4 Discussion**

3 Whilst conceptual tools are commonly applied for routing mass movements at medium and
4 broad scales, most of them use single values or rules as break criteria, disregarding the high
5 degree of uncertainty (e.g., Gamma, 2000; Wichmann and Becht, 2003; Huggel et al., 2002;
6 Horton et al., 2013; Blahut et al., 2010). `r.randomwalk` introduces a set of tools to deal with
7 uncertain break criteria in a flexible way, depending on the quality of rules or relationships
8 available. In general, empirical-statistical relationships represent rough simplifications as
9 mass movement processes may also stop when reaching valleys of higher order, run against
10 opposite slopes or loose energy when bending sharply. However, relatively robust rules or
11 relationships exist for the most common types of processes such as rock avalanches
12 (Scheidegger, 1973; see Fig. 5) or debris flows (Rickenmann, 1999). They build on data sets
13 large enough to derive meaningful envelopes and to compute impact indicator indices with
14 `r.randomwalk`. Relationships for less frequent types of processes are less robust as it was
15 illustrated for GLOFs (Haeberli, 1983; Zimmermann; 1997; Huggel et al., 2002; Huggel,
16 2004; see Sect. 3.3.2). In such cases we recommend to compute impact indicator scores
17 building on more than one model, as shown by Gruber and Mergili (2013) and in the present
18 work. Impact indicator indices and scores are mainly useful for anticipating the possible
19 impact area of expected single events (see Sect. 3.1.2), or for application at broader scales
20 (see Sect. 3.3.2).

21 The impact probability is useful for predicting possible impact areas of mass movements in
22 areas where many events are documented, but the volumes of possible future events are not
23 known. Whilst in the present paper it was demonstrated how to compute impact probabilities
24 related to observed release areas, `r.randomwalk` also includes the option to combine the
25 impact probability with the release probability P_R (see Table 1). Landslide release probability
26 (susceptibility) maps are often produced from a landslide inventory and a set of
27 environmental layers (e.g., Guzzetti, 2006). Starting random walks from each single pixel of a
28 study area, and combining the release probability of this pixel with the impact probability
29 allows to produce a composite probability $P_{I,C}$ map. Doing this is non-trivial and requires
30 specific strategies. It is therefore covered in a separate article (Mergili and Chu, 2015). Gruber
31 and Mergili (2013) have combined release and impact indicator scores for various types of

1 high-mountain hazards, and overlaid the results with a land cover data set to produce a risk
2 indicator score.

3 The sensitivity of r.randomwalk to variations of the parameters n_{walks} , R_{max} , f_{β} , f_d , L_{ctrl} , L_{seg} (see
4 Sect. 2.2) and the pixel size were tested for the Acheron Rock Avalanche. Even though the
5 optimized values are applied also to the other cases in the present work, this issue requires
6 further investigation, also with regard to the scale of the processes. This is particularly true for
7 the pixel size which has to be fine enough not to lose the geometrical characteristics
8 governing the motion (Blahut et al., 2010). Furthermore, coarser pixels and a larger number of
9 random walks make results more conservative. R_{max} , f_{β} and f_d control the degree of lateral
10 spreading and therefore influence the conservativeness of the results. In the future we plan to
11 compare the performance of r.randomwalk to software tools using multiple flow direction
12 algorithms (e.g., Flow-R; Horton et al., 2013) in terms of computational times and prediction
13 success.

14 Overestimating the travel distance at a certain pixel is avoided by choosing sufficiently high
15 values of L_{seg} (see Fig. 6C). Shorter travel distances at a certain pixel are associated to higher
16 values of ω and, consequently, larger predicted impact areas – i.e., more conservative results
17 which are desirable for many applications. The values of R_{max} leading to the best prediction
18 quality are considerably lower than run-up height observed for the Acheron Rock Avalanche.
19 This phenomenon is explained by the facts that (i) the observed maximum run-up height
20 refers to a limited area, whilst r.randomwalk applies the run-up height defined by R_{max} in any
21 place; and (ii) not all random walks reach the bottom of the valley before running up.

22 We have demonstrated how to estimate the prediction quality of III and P_1 maps. Where
23 sufficient reference data are available to prove the validity of the model, the results may be
24 applied for hazard zoning. Where not, the outcomes of r.randomwalk are suitable for broad-
25 scale overviews of possibly affected areas which have to be considered as rough indicators
26 only. A suitable level of spatial aggregation may be necessary in such cases (Gruber and
27 Mergili, 2013).

28 r.randomwalk includes a break criterion building on the two-parameter friction model of
29 Perla et al. (1980) (see Sect. 1 and Table 3) which can be used to compute flow velocities
30 (e.g., Wichmann and Becht, 2013; Mergili et al., 2012a; Horton et al., 2013). Evaluating this
31 functionality has to build on (i) specific strategies for the sensitivity analysis and optimization
32 of multiple parameters and (ii) a sound comparison with the outcome of physically-based

1 models. This effort will be presented in a separate article (Krenn et al., submitted). Further,
2 the parameter sensitivity and optimization code AIMEC (Fischer, 2013) can be directly
3 coupled to r.randomwalk.

4

5 **5 Conclusions**

6 We have introduced the open source GIS tool r.randomwalk, designed for conceptual
7 modelling of the propagation of mass movements. r.randomwalk comes up with built-in
8 functions for considering uncertainties and for validation. Employing a set of three
9 contrasting test areas, we have demonstrated (i) the possibility to combine results yielded with
10 various break criteria into one impact indicator score; (ii) the option to explore multiple
11 computational cores for combining the results obtained with many randomized parameter
12 combinations into an impact indicator index; (iii) the possibility to back-calculate the CDF of
13 the angles of reach of observed landslides, and to use this CDF to make forward predictions
14 of the impact probability; (iv) integrated functions for the validation and visualization of the
15 results. This includes strategies to properly separate the data sets for parameter optimization
16 and model validation.

17 We have further shown that controls for smoothing of the flow path and the avoidance of
18 circular flows have to be introduced to avoid underestimating travel distances and impact
19 areas. The number of random walks executed for each mass point and the pixel size influence
20 the level of conservativeness of the results rather than the quality of the prediction. The scope
21 of applicability of r.randomwalk strongly depends on the availability of robust break criteria
22 and on the availability of reference data for evaluation.

23

24 **Code availability**

25 The model codes, a user manual, the scripts used for starting the tests presented in Sect. 3 and
26 some of the test data are available at <http://www.mergili.at/randomwalk.html>.

27

28 **Acknowledgements**

1 The work was conducted as part of the international cooperation project “A GIS simulation
2 model for avalanche and debris flows” funded by the Austrian Science Fund (FWF) and the
3 German Research Foundation (DFG). Further, the support of Massimiliano Alvioli, Matthias
4 Benedikt, Yi-Chin Chen, Ivan Marchesini and Tim Davies is acknowledged.

5

6 **References**

- 7 Blahut, J., Horton, P., Sterlacchini, S. and Jaboyedoff, M.: Debris flow hazard modelling on
8 medium scale: Valtellina di Tirano, Italy. *Nat. Hazards Earth Syst. Sci.*, 10, 2379–2390,
9 2010. Haeberli, W.: Frequency and characteristics of glacier floods in the Swiss Alps. *Ann.*
10 *Glac.*, 4, 85–90, 1983.
- 11 Burton, A. and Bathurst, J. C.: Physically based modelling of shallow landslide sediment
12 yield at a catchment scale. *Environ. Geol.*, 35, 89–99, 1998.
- 13 Christen, C., Bartelt, P. and Kowalski, J.: Back calculation of the In den Arelen avalanche
14 with RAMMS: interpretation of model results. *Ann. Glac.*, 51(54), 161–168, 2010a.
- 15 Christen, M., Kowalski, J. and Bartelt, B.: RAMMS: Numerical simulation of dense snow
16 avalanches in three-dimensional terrain. *Cold Reg. Sci. Technol.*, 63, 1–14, 2010b.
- 17 Corominas, J.: The angle of reach as a mobility index for small and large landslides. *Canadian*
18 *Geotech. J.*, 33, 260–271, 1996.
- 19 Corominas, J., Copons, R., Vilaplana, J. M., Altamir, J. and Amigó, J.: Integrated Landslide
20 Susceptibility Analysis and Hazard Assessment in the Principality of Andorra. *Nat. Haz.*, 30,
21 421–435, 2003.
- 22 Evans, S. G., Roberts, N. J., Ischuk, A., Delaney, K. B., Morozova, G. S. and Tutubalina, O.:
23 Landslides triggered by the 1949 Khait earthquake, Tajikistan, and associated loss of life.
24 *Engin. Geol.*, 109, 195–212, 2009.
- 25 Fischer, J.-T.: A novel approach to evaluate and compare computational snow avalanche
26 simulation. *Nat. Haz. Earth Syst. Sci.*, 13, 1655–1667, 2013.
- 27 Gamma, P.: *Dfwalk – Murgang-Simulationsmodell zur Gefahrenzonierung*. Geographica
28 Bernensia, G66, 2000.

- 1 GRASS Development Team: Geographic Resources Analysis Support System (GRASS)
2 Software, Version 7.0. Open Source Geospatial Foundation, 2015. <http://grass.osgeo.org>, last
3 access: 27 July 2015.
- 4 Gruber, F. E. and Mergili, M.: Regional-scale analysis of high-mountain multi-hazard and
5 risk indicators in the Pamir (Tajikistan) with GRASS GIS. *Nat. Haz. Earth Syst. Sci.*, 13,
6 2779–2796, 2013.
- 7 Guo, D., Hamada, M., He, C., Wang, Y. and Zou, Y.: An empirical model for landslide travel
8 distance prediction in Wenchuan earthquake area. *Landslides*, 11, 281–291, 2014.
- 9 Guzzetti, F.: Landslide hazard and risk assessment. PhD Dissertation, Bonn, 2006.
- 10 Haeberli, W.: Frequency and characteristics of glacier floods in the Swiss Alps. *Ann. Glac.*,
11 4, 85–90, 1983.
- 12 Heim, A.: *Bergsturz und Menschenleben*. Fretz und Wasmuth, Zürich, 1932.
- 13 Hergarten, S. and Robl, J.: Modelling rapid mass movements using the shallow water
14 equations in Cartesian coordinates. *Nat. Haz. Earth Syst. Sci.*, 15, 671–685, 2015.
- 15 Horton, P., Jaboyedoff, M., Rudaz, B. and Zimmermann, M.: Flow-R, a model for
16 susceptibility mapping of debris flows and other gravitational hazards at a regional scale. *Nat.*
17 *Haz. Earth Syst. Sci.*, 13, 869–885, 2013.
- 18 Huggel, C.: Assessment of Glacial Hazards based on Remote Sensing and GIS Modeling.
19 Dissertation at the University of Zurich, Schriftenreihe Physische Geographie Glaziologie und
20 Geomorphodynamik, 2004.
- 21 Huggel, C., Käab, A., Haeberli, W., Teysseire, P. and Paul, F.: Remote sensing based
22 assessment of hazards from glacier lake outbursts: a case study in the Swiss Alps, *Can.*
23 *Geotech. J.*, 39, 316–330, 2002.
- 24 Huggel, C., Käab, A., Haeberli, W. and Krummenacher, B.: Regional-scale GIS-models for
25 assessment of hazards from glacier lake outbursts: evaluation and application in the Swiss
26 Alps. *Nat. Haz. Earth Syst. Sci.*, 3, 647–662, 2003.
- 27 Huggel, C., Haeberli, W., Käab, A., Bieri, D. and Richardson, S.: Assessment procedures for
28 glacial hazards in the Swiss Alps. *Can. Geotech.J.*, 41(6), 1068–1083, 2004a.

- 1 Huggel, C., Kääb, A. and Salzmann, N.: GIS-based modeling of glacial hazards and their
2 interactions using Landsat-TM and IKONOS imagery. *Norwegian J. Geog.*, 58, 761–773,
3 2004b.
- 4 Hungr, O., Corominas, J. and Eberhardt, E.: State of the Art paper: Estimating landslide
5 motion mechanism, travel distance and velocity. In: Hungr, O., Fell, R., Couture, R.,
6 Eberhardt, E. (eds.): *Landslide Risk Management. Proceedings of the International*
7 *Conference on Landslide Risk Management, Vancouver, Canada, 31 May – 3 June 2005,*
8 129–158, 2005.
- 9 Hungr, O.: A model for the runout analysis of rapid flow slides, debris flows, and avalanches.
10 *Can. Geotech. J.*, 32, 610–623, 2005.
- 11 Iverson, R. M.: The physics of debris flows. *Rev. Geophys.*, 35, 245–296, 1997.
- 12 Jibson R. W., Harp, E. L., Schulz, W. and Keefer, D. K.: Large rock avalanches triggered by
13 the M 7.9 Denali Fault, Alaska, earthquake of 3 November 2002. *Eng. Geol.*, 83, 144–160,
14 2006.
- 15 Kappes, M. S., Malet, J.-P., Remaître, A., Horton, P., Jaboyedoff, M., Bell, R.: Assessment of
16 debris-flow susceptibility at medium-scale in the Barcelonnette Basin, France. *Nat. Hazards*
17 *Earth Syst. Sci.*, 11, 627–641, 2011.
- 18 Krenn, J., Mergili, M., Fischer, J.-T., Davies, T., Frattini, P., Pudasaini, S. P.: Optimizing the
19 parameterization of mass flow models. Manuscript submitted to the Proceedings of the 12th
20 International Symposium on Landslides, Naples, Italy, 12–19 June 2016, 2015.
- 21 Kuo, Y. S., Tsai, Y. J., Chen, Y. S., Shieh, C. L., Miyamoto, K. and Itoh, T.: Movement of
22 deep-seated rainfall-induced landslide at Hsiaolin Village during Typhoon Morakot.
23 *Landslides*, 10(2), 191–202, 2013.
- 24 Legros, F.: The mobility of long-runout landslides, *Eng. Geol.*, 63, 301–331, 2002.
- 25 Lied, K. and Bakkehøi, S.: Empirical calculations of snow-avalanche run-out distance based
26 on topographic parameters. *J. Glaciol.*, 26, 165–177, 1980.
- 27 Lin, C. W., Chang, W. S., Liu, S. H., Tsai, T. T., Lee, S. P., Tsang, Y. C., Shieh, C. J. and
28 Tseng, C. M.: Landslides triggered by the 7 August 2009 Typhoon Morakot in southern
29 Taiwan. *Eng. Geol.*, 123(1), 3–12, 2011.

- 1 McClung, D. M. and Lied, K.: Statistical and geometrical definition of snow avalanche
2 runoff. *Cold Reg. Sci. Tech.*, 13, 107–119, 1987.
- 3 McDougall, S. and Hungr, O.: A Model for the Analysis of Rapid Landslide Motion across
4 Three-Dimensional Terrain. *Canadian Geotech. J.*, 41, 1084–1097, 2004.
- 5 McDougall, S. and Hungr, O.: Dynamic modeling of entrainment in rapid landslides.
6 *Canadian Geotech. J.*, 42, 1437–1448, 2005.
- 7 Mergili, M., and Chu, H.-J.: Integrated statistical modelling of spatial landslide probability.
8 *Nat. Haz. Earth Syst. Sci. Discuss.*, 3, 5677–5715, 2015.
- 9 Mergili, M. and Schneider, J. F.: Regional-scale analysis of lake outburst hazard in the
10 southwestern Pamir, Tajikistan, based on remote sensing and GIS. *Nat. Haz. Earth Syst. Sci.*,
11 11, 1447–1462, 2011.
- 12 Mergili, M., Schneider, D., Worni, R. and Schneider, J. F.: Glacial lake outburst floods in the
13 Pamir of Tajikistan: challenges in prediction and modelling. In: Genevois, R., Hamilton, D. L.
14 and Prestininzi, A. (eds.): *Proceedings of the 5th International Conference on Debris-Flow
15 Hazards Mitigation: Mechanics, Prediction and Assessment*, Padua, Italy, June 14-17, 2011.
16 *Italian J. Eng. Geol. Environ. – Book*, 973–982, 2011.
- 17 Mergili, M., Fellin, W., Moreiras, S. M. and Stötter, J.: Simulation of debris flows in the
18 Central Andes based on Open Source GIS: Possibilities, limitations, and parameter sensitivity.
19 *Nat. Haz.*, 61(3), 1051–1081, 2012a.
- 20 Mergili, M., Schratz, K., Ostermann, A. and Fellin, W.: Physically-based modelling of
21 granular flows with Open Source GIS. *Nat. Haz. Earth Syst. Sci.*, 12, 187–200, 2012b.
- 22 Mergili, M., Müller, J. P. and Schneider, J. F.: Spatio-temporal development of high-
23 mountain lakes in the headwaters of the Amu Darya river (Central Asia). *Glob. Plan. Change*,
24 107, 13–24, 2013.
- 25 Mergili, M., Marchesini, I., Alvioli, M., Metz, M., Schneider-Muntau, B., Rossi, M. and
26 Guzzetti, F.: A strategy for GIS-based 3D slope stability modelling over large areas. *Geosci.
27 Model Dev.*, 7, 2969–2982, 2014.
- 28 Mergili, M., Fischer, J.-T., Fellin, W., Ostermann, A. and Pudasaini, S. P.: An advanced open
29 source computational framework for the GIS-based simulation of two-phase mass flows and
30 process chains. *Geophys. Res. Abs.*, 17, EGU General Assembly, Vienna, April 12-17, 2015.

1 Neteler, M. and Mitasova, H.: Open source GIS: a GRASS GIS approach. Springer, New
2 York, 2007.

3 Pearson, K.: The Problem of the Random Walk. *Nature*, 72, 294, 1905.

4 Perla, R., Cheng, T. T. and McClung, D. M.: A Two-Parameter Model of Snow Avalanche
5 Motion. *J. Glaciol.*, 26, 197–207, 1980.

6 Pitman, E. B. and Le, L.: A two-fluid model for avalanche and debris flows. *Phil. Trans. R.*
7 *Soc. A363*, 1573–1601, 2005.

8 Pudasaini, S. P.: A general two-phase debris flow model, *J. Geophys. Res.*, 117, F03010,
9 2012.

10 Pudasaini, S. P. and Hutter, K.: *Avalanche Dynamics: Dynamics of rapid flows of dense*
11 *granular avalanches*. Springer, Berlin, Heidelberg, 2007.

12 R Core Team.: *R: A Language and Environment for Statistical Computing*. R Foundation for
13 *Statistical Computing*, Vienna, Austria, <http://www.R-project.org>, last access: 27 July 2014.

14 Rickenmann, D.: Empirical Relationships for Debris Flows. *Nat. Haz.*, 19, 47–77, 1999.

15 Savage, S. B. and Hutter, K.: The motion of a finite mass of granular material down a rough
16 incline. *J. Fluid Mech.*, 199, 177–215, 1989.

17 Scheidegger, A. E.: On the Prediction of the Reach and Velocity of Catastrophic Landslides.
18 *Rock Mech.*, 5, 231–236, 1973.

19 Scheidl, C., Rickenmann, D.: Empirical prediction of debris-flow mobility and deposition on
20 fans. *Earth Surf. Proc. Landforms*, 35(2), 157–173, 2010.

21 Smith, G. M., Davies, T. R., McSaveney, M. J. and Bell, D. H.: The Acheron rock avalanche,
22 Canterbury, New Zealand – morphology and dynamics. *Landslides*, 3, 62-72, 2006.

23 Sosio, R., Crosta, G.B., Chen J.H. and Hungr, O.: Modelling rock avalanche propagation onto
24 glaciers. *Quat. Sci. Rev.*, 47, 23–40, 2012.

25 Takahashi, T., Nakagawa, H., Harada, T. and Yamashiki, Y.: Routing debris flows with
26 particle segregation. *J. Hydr. Res.*, 118(11), 1490–1507, 1992.

27 Van Westen, C. J., van Asch, T. W. J. and Soeters, R.: Landslide hazard and risk zonation :
28 why is it still so difficult? *Bull. Eng. Geol. Environ*, 65(2), 176–184, 2005.

- 1 Vandre, B. C.: Rudd Creek debris flow. In: Bowles, D.S. (eds.): Delineation of landslide,
2 flash flood and debris flow hazards in Utah, 117–131. Utah Water Research Laboratory,
3 1985.
- 4 Voellmy, A.: Über die Zerstörungskraft von Lawinen. Schweizerische Bauzeitung 73, 159–
5 162, 212–217, 246–249, 280–285, 1955.
- 6 Wichmann, V. and Becht, M.: Modelling of Geomorphic Processes in an Alpine Catchment.
7 In: Proceedings of the 7th International Conference on GeoComputation, Southampton, 2003.
- 8 Wu, C. H., Chen, S. C. and Chou, H. T.: Geomorphologic characteristics of catastrophic
9 landslides during typhoon Morakot in the Kaoping Watershed, Taiwan. Engineering Geology,
10 123, 13–21, 2011.
- 11 Zimmermann, M., Mani, P. and Gamma, P.: Murganggefahr und Klimaänderung – ein GIS
12 basierter Ansatz. NFP 31 Schlussbericht, Hochschulverlag an der ETH, Zürich, 1997.
- 13

1 Table 1. Summary of the key variables used in r.randomwalk.

Symbol	Unit [Range]	Name	Description / Remarks
Input			
n_{walks}	- [≥ 0]	Size of a set of walks	Logarithm (base of 10) of the number of random walks
L_{ctrl}	m [> 0]	Control length	Backward distance of each step of a random walk over which the horizontal distance of motion has to increase (see Fig. 2A)
L_{seg}	m [> 0]	Segment length	Length of segments used for computing L_{max} (see Fig. 2B)
R_{max}	m [≥ 0]	Maximum vertical run-up height	-
f_d	- [> 0]	Direction factor	Factor for weighting the perpetuation of the movement direction during routing
f_β	- [≥ 0]	Slope factor	Factor for weighting the slope during routing
V	m ³ [> 0]	Movement volume	-
Q_p	m ³ /s [> 0]	Peak discharge	Applicable to lake outburst events (see Table 3)
a, b, c	- []	-	Parameters needed by the rules and relationships applied (see Table 3)
P_R	- [0–1]	Release probability	Spatial probability that a mass movement is released from a given pixel (Mergili and Chu, 2015)
RIS	- [≥ 0]	Release indicator score	Ordinal score denoting the tendency of a pixel to produce a mass movement
EIS	- [≥ 0]	Exposure indicator score	Ordinal score denoting the exposed values at a given pixel
Output			

L_{\max}	$m [\geq 0]$	Travel distance	Horizontal distance between the release pixel and the most distant pixel reached by a set of random walks, measured along the segments of the path (see Fig. 2B)
Z	$m [\geq 0]$	Elevation loss	Vertical distance between the release pixel and the most distant pixel reached by a set of random walks
ω_T	$^\circ [< 90]$	Angle of reach	Average slope angle measured between the release pixel and the most distant pixel reached by a set of random walks
IF	$- [\geq 0]$	Impact frequency	Number of random walks impacting a given pixel
IIS	$- [\geq 0]$	Impact indicator score	Number of rules and relationships predicting an impact on a given pixel
$IHIS$	$- [\geq 0]$	Impact hazard indicator score	Ordinal score serving as a qualitative surrogate for the hazard of an impact on a given pixel
III	$- [0-1]$	Impact indicator index	Fraction of model runs impacting a given pixel out of all model runs
P_I	$- [0-1]$	Impact probability	Spatial probability that a given pixel is impacted, building on user-defined release areas and a cumulative density function
$P_{I,C}$	$- [0-1]$	Composite probability	Spatial probability that a given pixel is impacted, building on P_R and P_I (Mergili and Chu, 2015)
$IRIS$	$- [\geq 0]$	Impact risk indicator score	Ordinal score denoting the expected/potential loss at a given pixel

1

2

1 Table 2. Possibilities to define the break criteria. The flags provided through the command
 2 line or the user interface define the type of break criterion. RC = release coordinates (release
 3 from highest points of release areas), RP = release pixels (release from all pixels within
 4 release areas), ● = relevant for most applications, ○ = relevant for some applications.

Flag	Mode	Release		Output	Validation	Multiple cores
		RC	RP			
q	Published relationships (see Table 3)	●		IIS	○	
m	Published relationship, multiple runs	●		III	○	●
p	Impact probability	○	○	P_1	○	
p+n	Impact probability, multiple runs	○	○	P_1	●	●
b	Reconstruction of observation	○	○	CDF		

5

6

1 Table 3. Types of rules and relationships supported by r.randomwalk. ω_T = angle of reach,
 2 L_{\max} = travel distance, V = volume of motion, Z = elevation loss, Q_p = peak discharge at
 3 release, v_T = velocity at termination.

ID	Equation	Examples				
		Reference	Process	a	b	c
1	$\omega_T = a$ (2)	Haeberli (1983); Huggel et al. (2002)	Debris flow from GLOF	11		
2	$\log_{10} \tan \omega_T = a \log_{10} V + b$ (3)	Scheidegger (1973)	Rock avalanch e	-0.15666	0.62419	
3	$L_{\max} = aV^bZ^c$ (4)	Rickenmann (1999)	Debris flow	1.9	0.16	0.83
4	$\omega_T = aQ_p^b$ (5)	Huggel (2004)	GLOF	18	-0.07	
5	$v_T \leq 0$ (6)	Perla et al. (1980)				

4

5

1 Table 4. Tests of the parameters n_{walks} , L_{ctrl} , L_{seg} , R_{max} , f_{β} , f_{d} and the pixel size. Where ranges
2 of values are given in bold, the model is run with 100 random samples constrained by the
3 minima and maxima indicated. Where values given in bold are separated by commas, exactly
4 these values are tested. Test criteria: ¹ impact area, ² travel distance L_{max} (flag b), ³ AUC_{ROC} .

Test	n_{walks}	L_{ctrl} (m)	L_{seg} (m)	R_{max} (m)	f_{β}	f_{d}	Pixel size (m)
1 ^{1,3}	$10^0 - 10^6$	1000	100	10	5	2	10, 20, 40
2 ²	10^4	50, 1000	10–150	1000	5	2	10, 20, 40
3 ^{1,2,3}	10^4	50–1000² 1000–4000^{1,3}	100	1000 ² $10^{1,3}$	5	2	10, 20, 40² $20^{1,3}$
4 ^{1,3}	10^4	1000	100	0–120	5	2	20
5 ^{1,3}	10^4	1000	100	10	0–10	2	20
6 ^{1,3}	10^4	1000	100	10	5	1–10	20

5

6

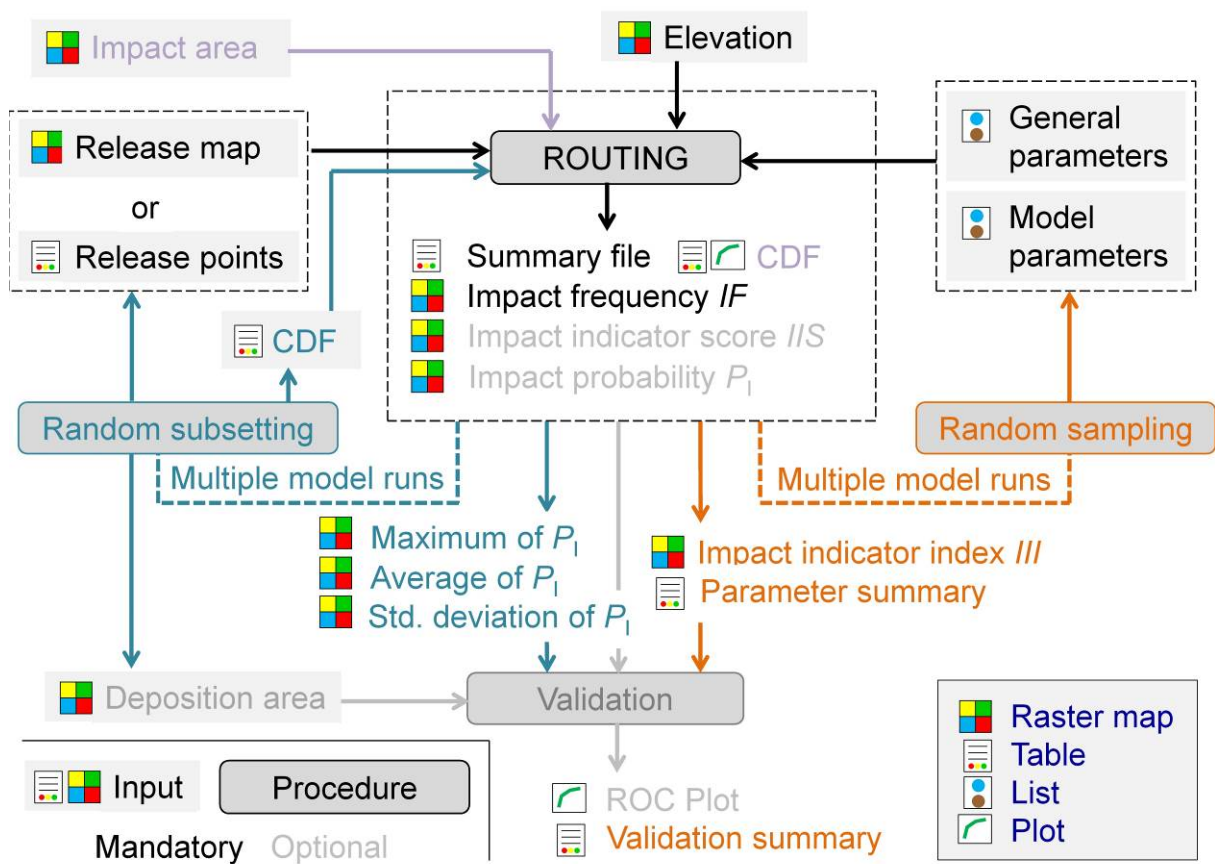
1 Table 5. Empirical-statistical relationships and simple rules used for computing the IIS of
 2 GLOFs in the Gunt Valley (see Table 3). ^{1,2} ID(s) of test(s) where the rule or relationship is
 3 applied. ³ A bulking factor of 5 is applied to V (modified after Iverson, 1997).

IDTest	Relationship	Reference	Process
1 ¹	$\omega_T = 11^\circ$	Haeberli (1983); Zimmermann et al. (1997); Huggel et al. (2003, 2004)	Flood or debris flow
1 ²	$\omega_T = 7^\circ$	Zimmermann et al. (1997)	
2 ^{1,2}	$\omega_T = 18Q_p^{-0.07}$	Huggel (2004)	
3 ^{1,2}	$L_{\max} = 1.9V^{0.16}Z^{0.83}$	Rickenmann (1999) ³	
4 ^{1,2}	$\omega_T = 6^\circ$		Flood
5 ^{1,2}	$\omega_T = 4^\circ$		
6 ^{1,2}	$\omega_T = 2^\circ$	Haeberli et al. (1983); Huggel et al. (2004)	

4

5

1 **Figures**

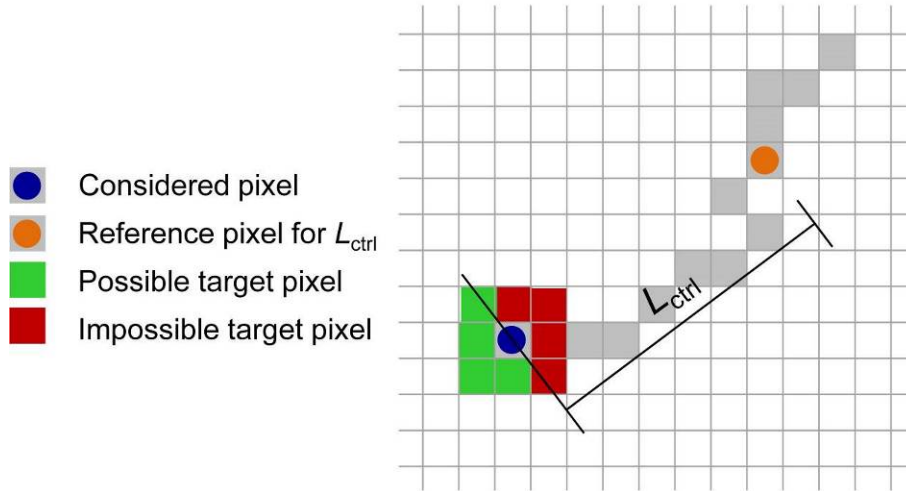


2

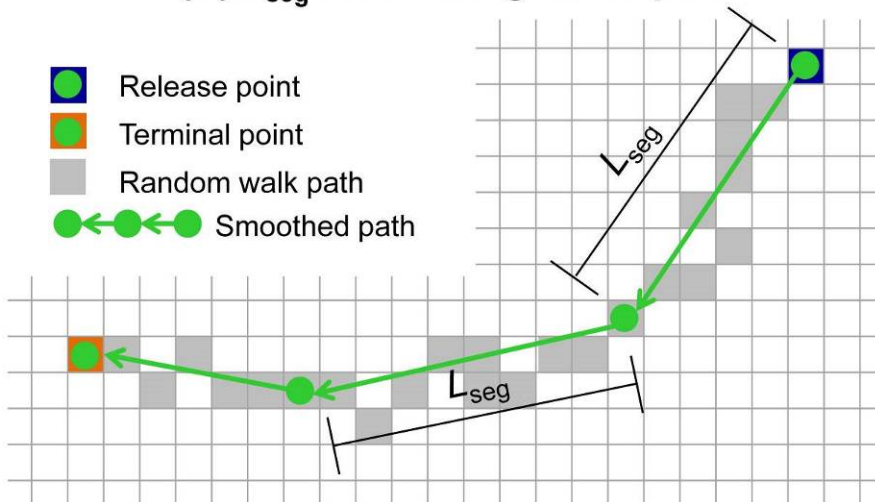
3 Figure 1. Logical framework of *r.randomwalk*. Only those components covered in the present
 4 article are shown.

5

(A) L_{ctrl} : avoidance of sharp bending



(B) L_{seg} : smoothing of the path

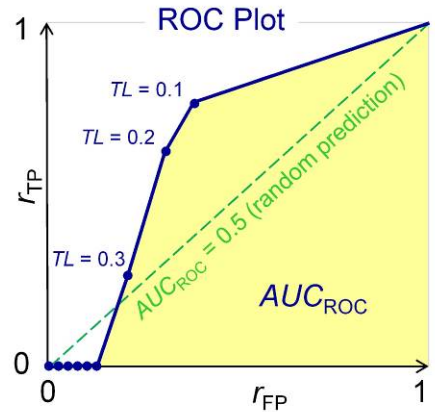
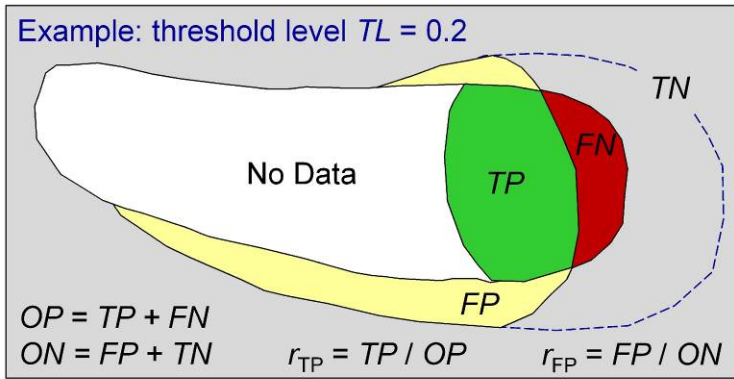
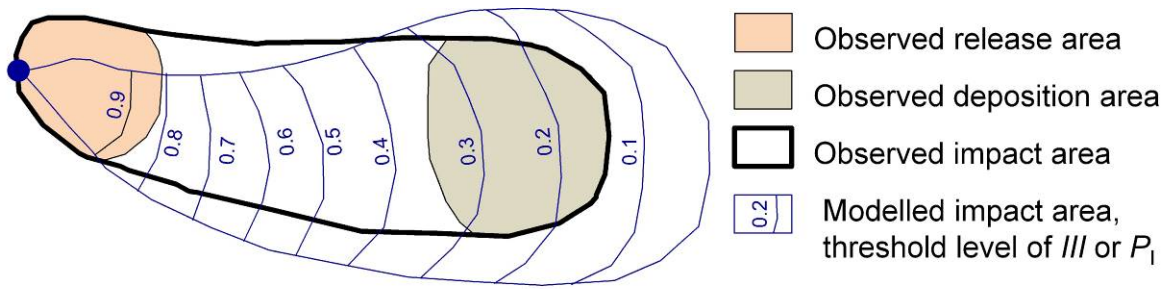


2

3 Figure 2. Control length L_{ctrl} and segment length L_{seg} . (A) Application of L_{ctrl} to avoid sharp
 4 bending of the flow. (B) Smoothing of the flow path by introducing segments with maximum
 5 length of L_{seg} .

6

1

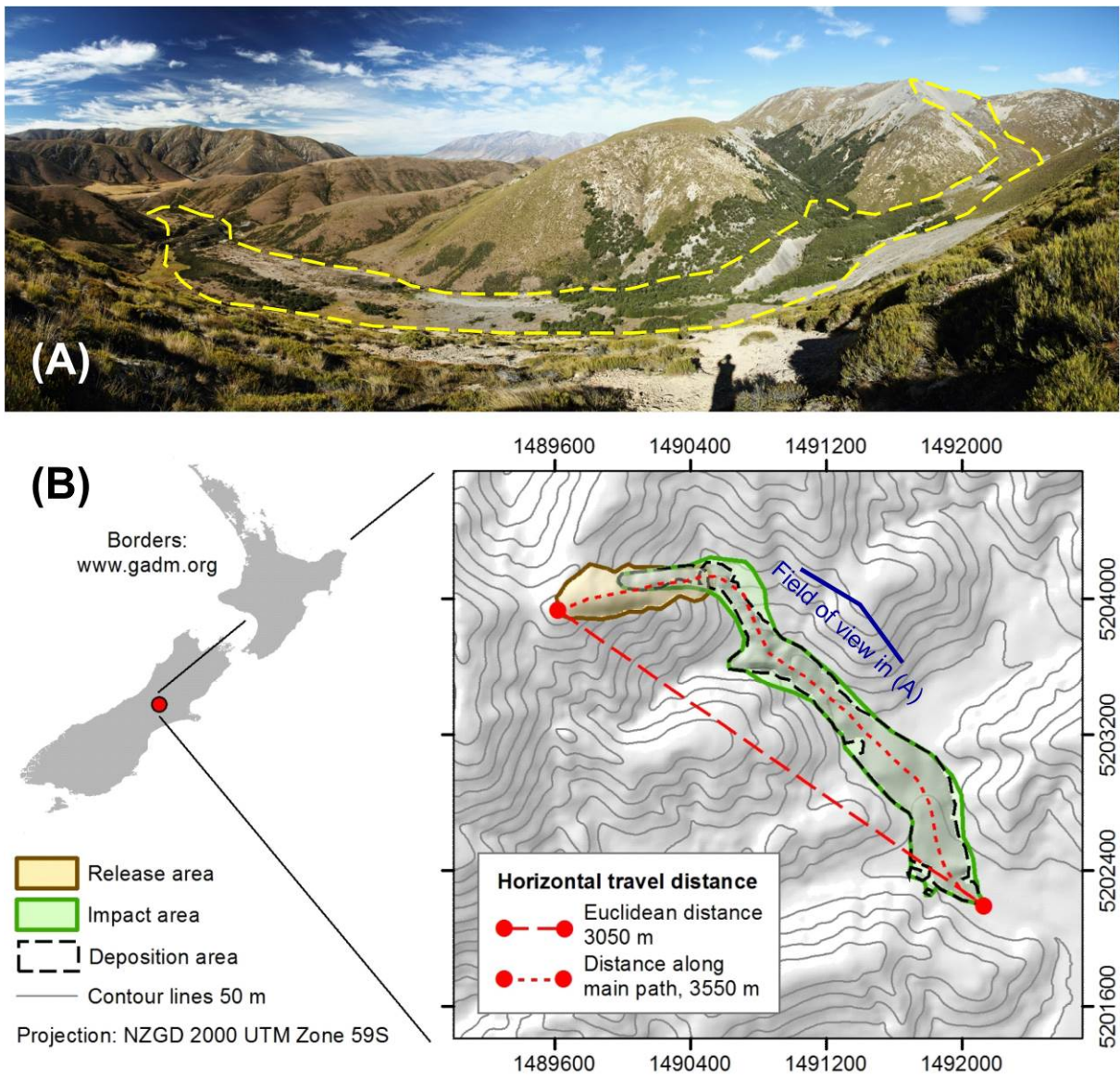


2

3 Figure 3. Model validation with an ROC Plot, relating the false positive rate r_{FP} and the true
 4 positive rate r_{TP} . This way of validation is suitable for predictor raster maps in the range 0–1,
 5 such as III or P_1 . It can also be used for binary predictor maps (0 or 1). In such a case AUC_{ROC}
 6 is computed from two threshold levels only.

7

1



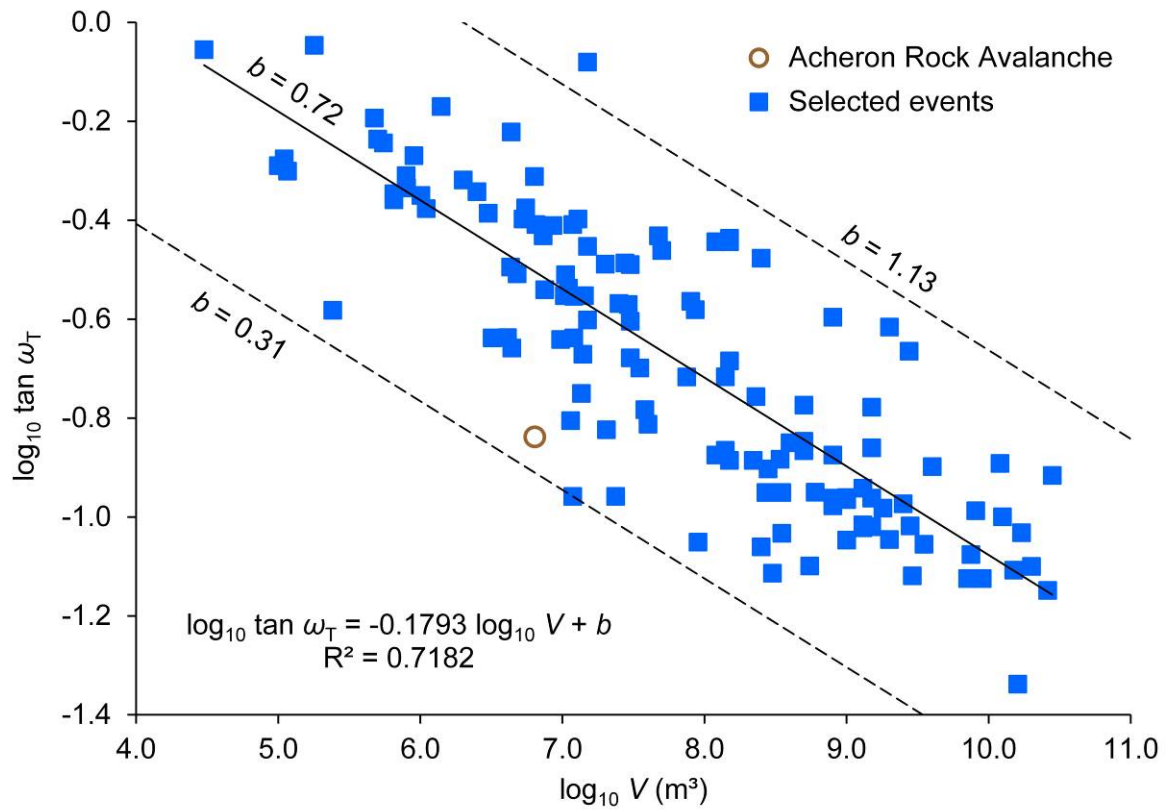
2

3 Figure 4. Acheron Rock Avalanche. (A) Panoramic view, photo: M. Mergili, 28 February

4 2015. (B) Location and geometry.

5

1

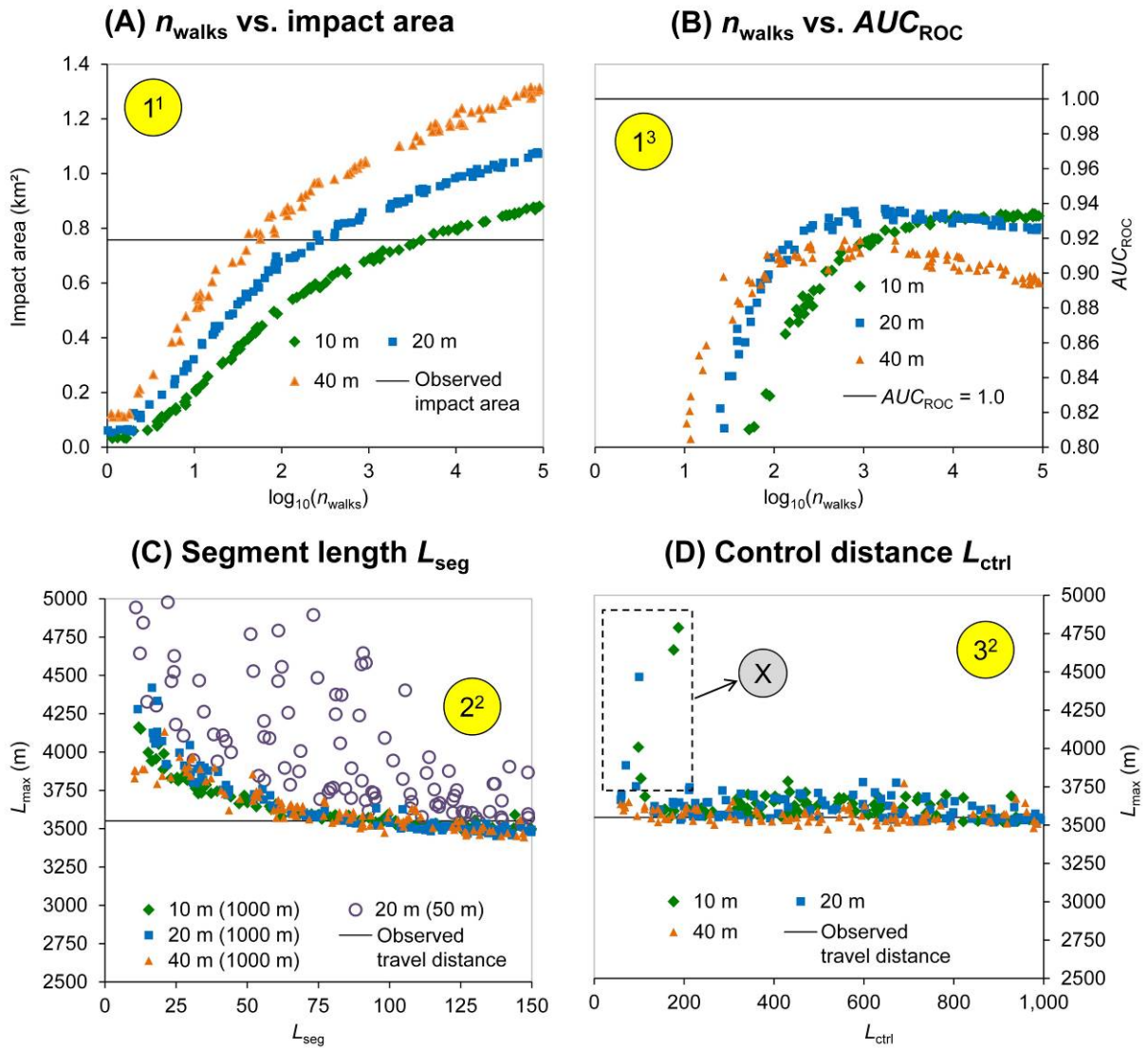


2

3 Figure 5. Empirical-statistical relationship relating the angle of reach ω_T to the volume V of
4 avalanching flows of rock or debris. The data are compiled from Scheidegger (1973); Legros
5 (2002); Jibson et al. (2006); Evans et al. (2009); Sosio et al. (2012); Guo et al. (2014).

6

1

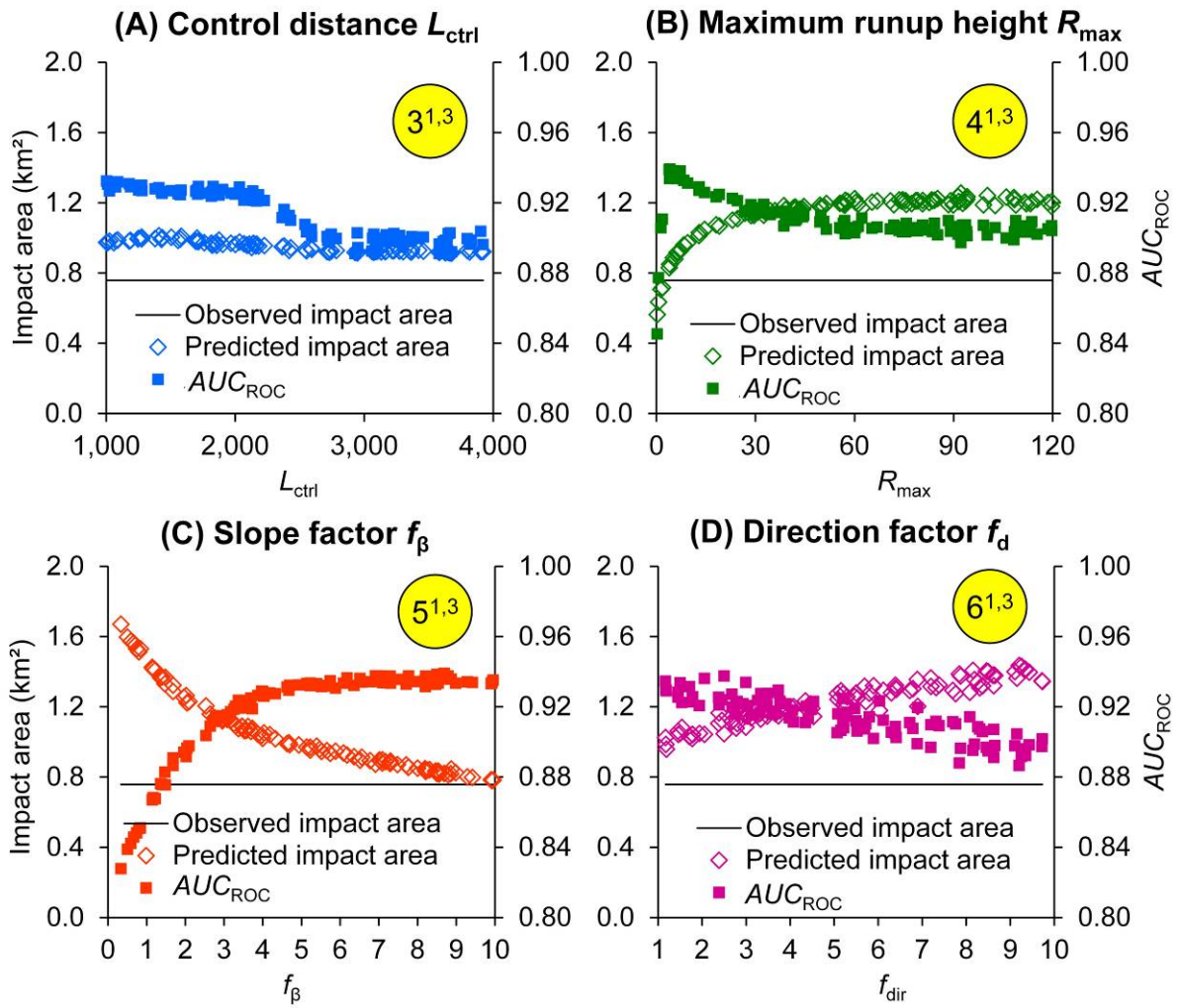


2

3 Figure 6. Results of the Tests 1–3 (number of test indicated in the yellow circle). Number of
 4 random walks plotted against (A) the impact area and (B) the area under the ROC Curve. (C)
 5 Computed travel distance L_{\max} as a function of L_{seg} (in the legend, the corresponding value of
 6 L_{ctrl} is given in brackets). (D) Computed L_{\max} as a function of L_{ctrl} .

7

1

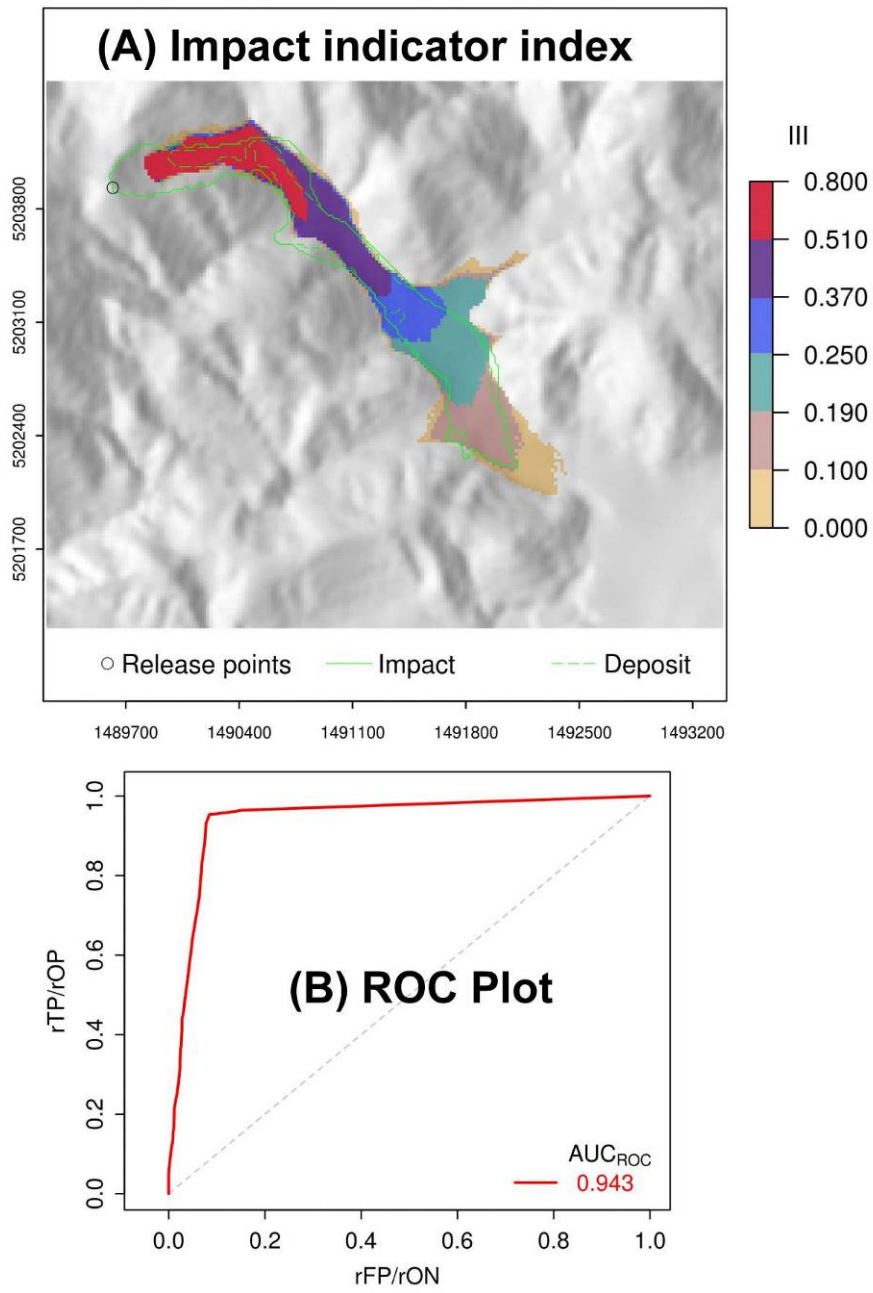


2

3 Figure 7. Sensitivity of impact area and AUC_{ROC} to selected input parameters. The numbers of
 4 the corresponding tests (see Table 4) are indicated in the yellow circles. (A) Control distance
 5 L_{ctrl} . (B) Maximum run-up height R_{max} . (C) Slope factor f_{β} . (D) Direction factor f_d .

6

1



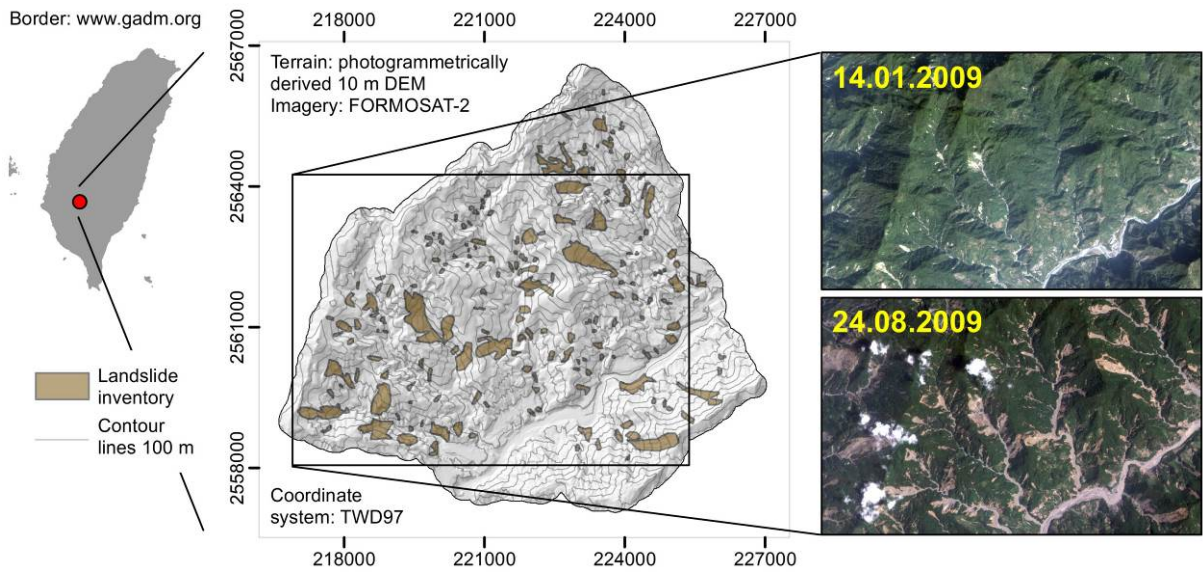
2

3 Figure 8. Impact indicator score for the Acheron Rock Avalanche. (A) Classified III map. (B)

4 ROC Plot, building on normalized ON area (see Sect. 2.5).

5

1

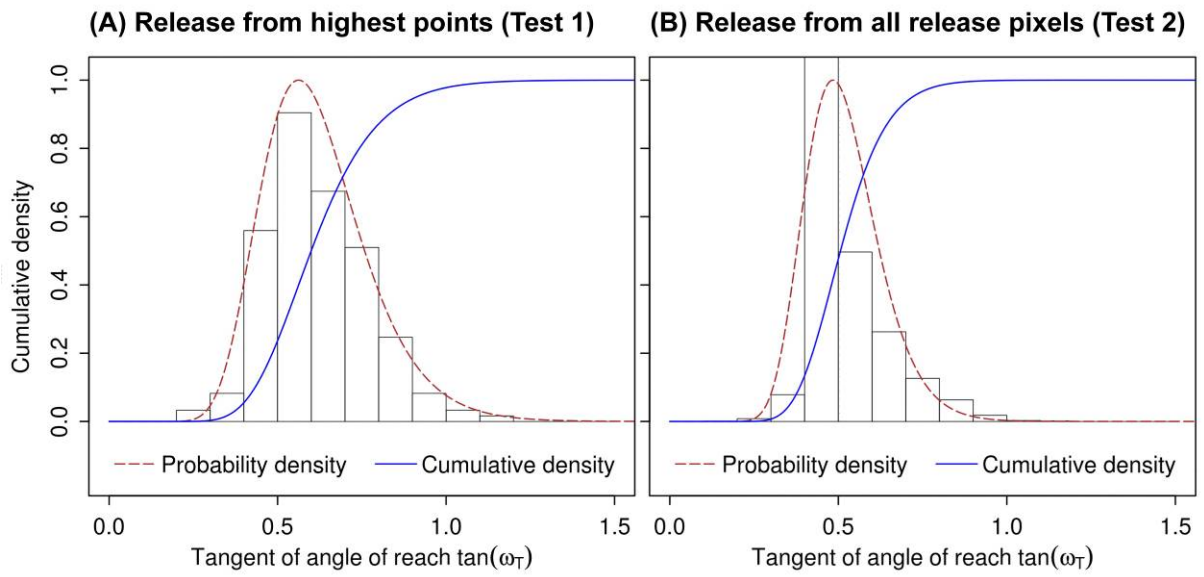


2

3 Figure 9. Location, terrain and landslide inventory of the Kao Ping Watershed, Taiwan.
4 Comparison of the satellite images illustrates the landslide-induced land cover changes
5 associated with the Typhoon Morakot. The landslide inventory builds on the interpretation of
6 the FORMOSAT-2 imagery.

7

1

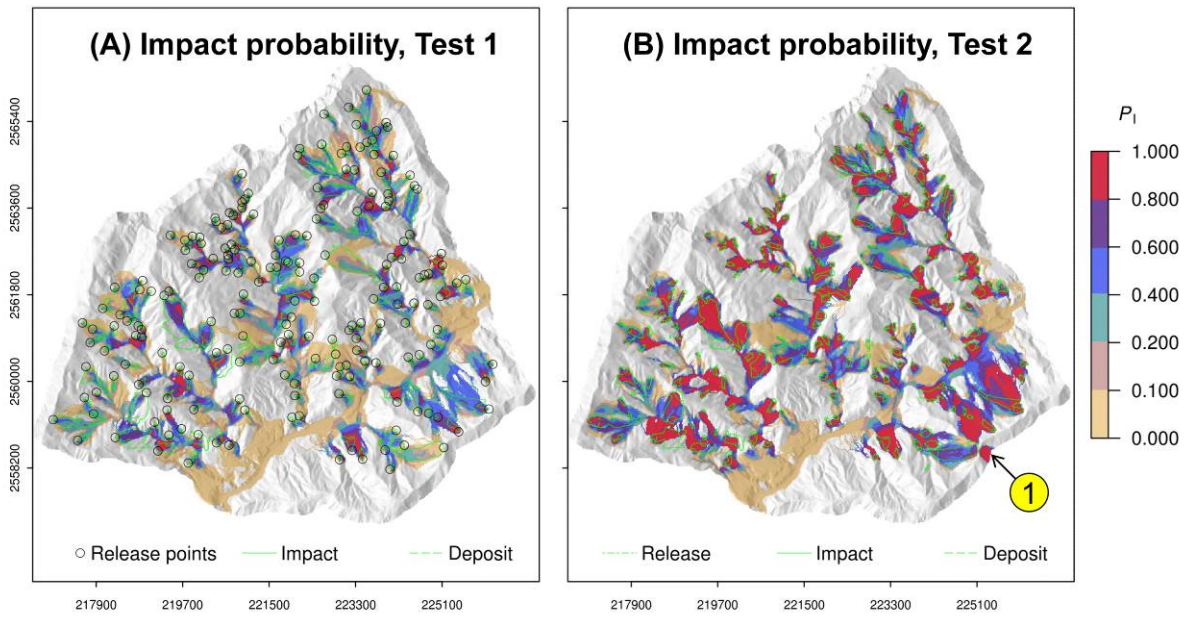


2

3 Figure 10. Histograms, probability densities and cumulative densities of ω_T of mass
4 movements in the test area in the Kao Ping Watershed. (A) Result for a set of 10^4 random
5 walks started from the highest point of each landslide (Test 1). (B) Result for a set of 10^4
6 random walks started from each pixel within the release areas of all landslides (Test 2).

7

1

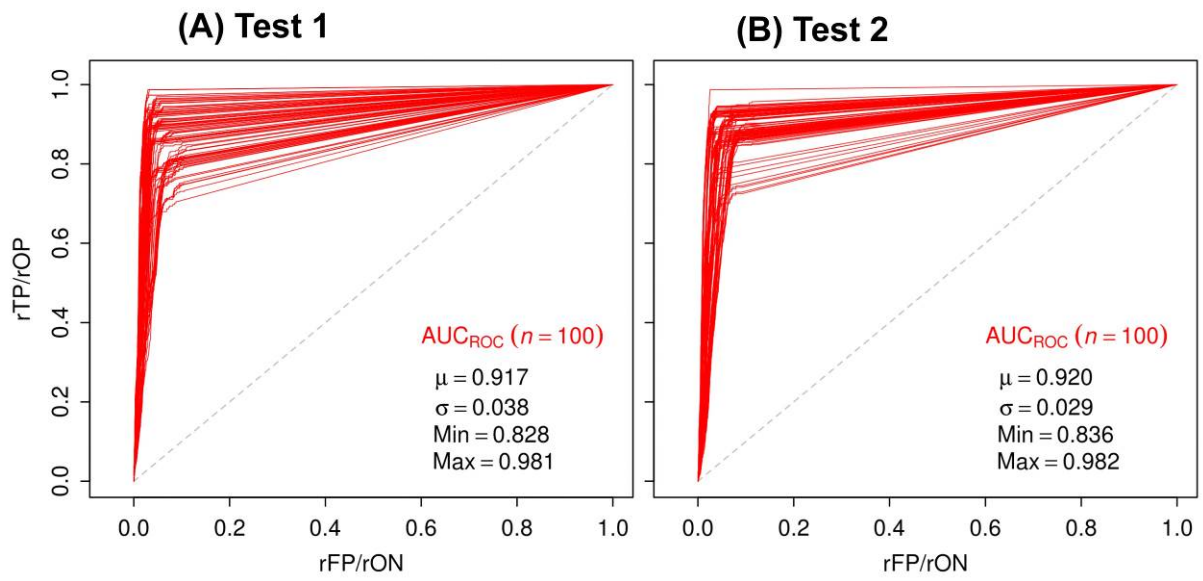


2

3 Figure 11. Impact probability in the range 0–1. (A) Result of Test 1 (random walks starting
4 from the highest point of each landslide, cumulative density according to Fig. 10A). (B)
5 Result of Test 2 (random walks starting from all release pixels, cumulative density according
6 to Fig. 10B).

7

1

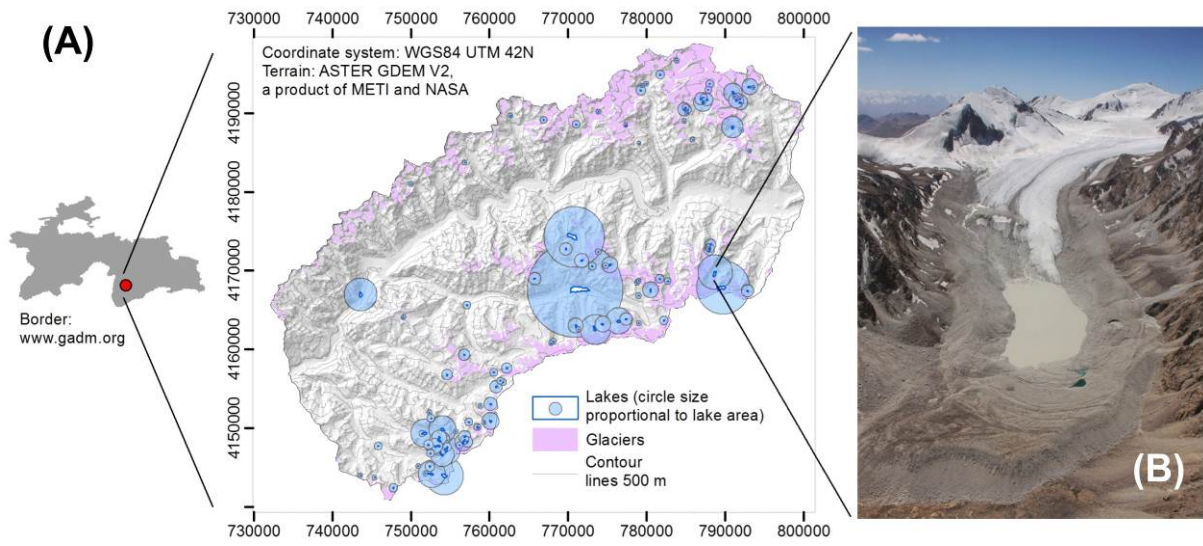


2

3 Figure 12. ROC Plots illustrating the prediction quality of (A) Test 1 and (B) Test 2, using the
4 original number of TN pixels (see Sect. 2.5).

5

1

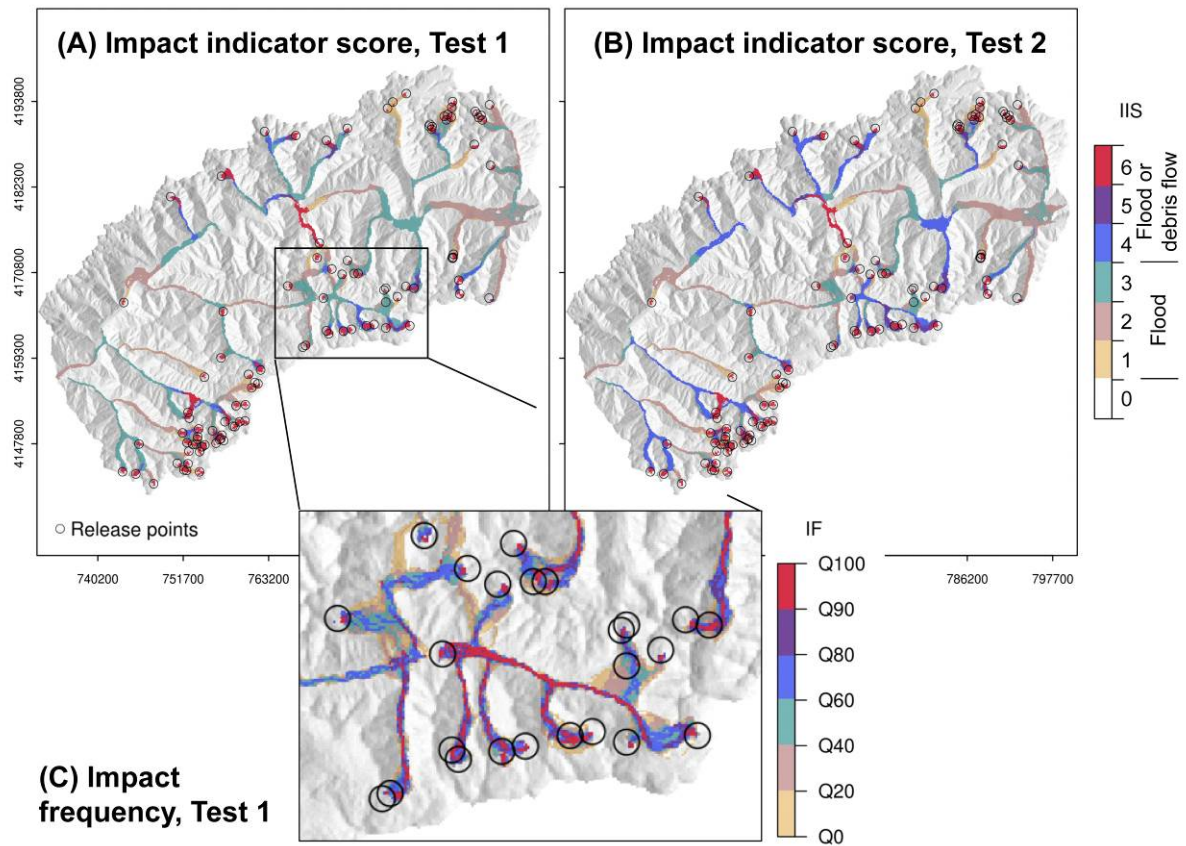


2

3 Figure 13. The test area in the Gunt Valley, Tajikistan. (A) Location, topography, glaciers and
4 lakes. (B) Proglacial lake in the upper Varshedzdara Valley, photo: M. Mergili, 18 August
5 2011.

6

1



2

3 Figure 14. Possible GLOF impact areas in the Gunt Valley, Tajikistan. (A) Impact indicator
4 score derived with Test 1. (B) Impact indicator score derived with Test 2. (C) Impact
5 frequency derived with Test 1, classified by quantiles.